


















Self-Consistent JWST Census of Star Formation and AGN activity at $z = 5.5 - 13.5$

JORDAN C. J. D'SILVA ^{1,2} SIMON P. DRIVER ¹ CLAUDIA D. P. LAGOS ^{1,2} AARON S. G. ROBOTHAM ¹
NATHAN J. ADAMS ³ CHRISTOPHER J. CONSELICE ³ BRENDA FRYE ⁴ NIMISH P. HATHI ⁵ THOMAS HARVEY ³
RAFAEL ORTIZ III ⁶ MASSIMO RICOTTI ⁷ CLAYTON ROBERTSON ⁸ ROSS M. SILVER ⁹ STEPHEN M. WILKINS ¹⁰
CHRISTOPHER N. A. WILLMER ¹¹ ROGIER A. WINDHORST ⁶ SETH H. COHEN ⁶ ROLF A. JANSEN ⁶
JAKE SUMMERS ⁶ ANTON M. KOEKEMOER ¹² DAN COE ^{12,13,14} NORMAN A. GROGIN ¹²
MADELINE A. MARSHALL ¹⁵ MARIO NONINO ¹⁶ NOR PIRZKAL ¹² RUSSELL E. RYAN, JR. ¹² AND HAOJING YAN ¹⁷

- ¹International Centre for Radio Astronomy Research (ICRAR) and the International Space Centre (ISC), The University of Western Australia, M468, 35 Stirling Highway, Crawley, WA 6009, Australia
²ARC Centre of Excellence for All Sky Astrophysics in 3 Dimensions (ASTRO 3D), Australia
³Jodrell Bank Centre for Astrophysics, Alan Turing Building, University of Manchester, Oxford Road, Manchester M13 9PL, UK
⁴Department of Astronomy/Steward Observatory, University of Arizona, 933 N Cherry Ave, Tucson, AZ, 85721-0009, USA
⁵Space Telescope Science Institute, 3700 San Martin Drive, Baltimore, MD 21210, USA
⁶School of Earth and Space Exploration, Arizona State University, Tempe, AZ 85287-1404, USA
⁷Department of Astronomy, University of Maryland, College Park, 20742, USA
⁸Department of Physics and Astronomy, University of Louisville, Natural Science Building 102, Louisville, KY 40292, USA
⁹Astrophysics Science Division, NASA Goddard Space Flight Center, Greenbelt, MD 20771, USA
¹⁰Astronomy Centre, University of Sussex, Falmer, Brighton BN1 9QH, UK
¹¹Steward Observatory, University of Arizona, 933 N Cherry Ave, Tucson, AZ, 85721-0009, USA
¹²Space Telescope Science Institute, 3700 San Martin Drive, Baltimore, MD 21218, USA
¹³Association of Universities for Research in Astronomy (AURA) for the European Space Agency (ESA), STScI, Baltimore, MD 21218, USA
¹⁴Center for Astrophysical Sciences, Department of Physics and Astronomy, The Johns Hopkins University, 3400 N Charles St. Baltimore, MD 21218, USA
¹⁵Los Alamos National Laboratory, Los Alamos, NM 87545, USA
¹⁶INAF-Osservatorio Astronomico di Trieste, Via Bazzoni 2, 34124 Trieste, Italy
¹⁷Department of Physics and Astronomy, University of Missouri, Columbia, MO 65211, USA

ABSTRACT

The cosmic star formation history (CSFH) and cosmic active galactic nuclei (AGN) luminosity history (CAGNH) are self consistently presented at $z = 5.5 - 13.5$. This is achieved by analyzing galaxies detected by the James Webb Space Telescope from ≈ 400 arcmin² fields from the PEARLS, CEERS, NGDEEP, JADES and PRIMER surveys. In particular, the combination of spectral energy distribution fitting codes, EAZY and PROSPECT, are employed to estimate the photometric redshifts and astrophysical quantities of 3947 distant galaxies, from which we compute the stellar mass, star formation rate and AGN luminosity distribution functions in four redshift bins. Integrating the distribution functions, we find that the CAGNH tentatively rises by ≈ 2.2 dex over $z = 5.5 - 13.5$ compared to ≈ 1.8 dex for the CSFH, indicating that the growth of supermassive black holes (SMBHs) tends to outpace the assembly of stellar mass. We connect our results of the CSFH and CAGNH at $z = 5.5 - 13.5$ to that from $z = 0 - 5$ to determine the summary of $\gtrsim 13$ Gyr of star formation and AGN activity, from the very onset of galaxy formation to the present day.

1. INTRODUCTION

Two of the most important physical processes occurring in galaxies are the assembly of stellar mass and the growth of supermassive black holes (SMBHs) powering active galactic nuclei (AGN). The prominence of these two processes is inferred by their relative contributions to the spectral energy distributions (SEDs) of galaxies at

virtually all wavelengths from the X-rays through to the radio (e.g., Conroy 2013; Padovani et al. 2017). Because of their similar contributions to the SED, inferences on the physics of star formation rely on appropriately accounting for the AGN component and vice-versa.

Often, the strategy is to separate galaxies into either star forming or AGN with diagnostic parameters such as optical emission lines (e.g., the BPT diagram, Baldwin et al. 1981) and X-ray emission (e.g., Brandt & Alexander 2015). Especially at high redshift, this strategy does not work well. Common emission line ratios cannot significantly separate AGN from star-forming galaxies in the low metallicity terrain of the $z \gtrsim 5$ Universe (Maiolino et al. 2023; Übler et al. 2023) and X-ray detections of confirmed broad-line $z \gtrsim 5$ AGN are sparse, suggesting either significant X-ray absorption or naturally X-ray faint AGN (Ananna et al. 2024; Yue et al. 2024).

The current paradigm of vast multiwavelength surveys has afforded the ability to simultaneously treat star formation and AGN when interpreting the emission of galaxies. Using the multiwavelength Galaxy and Mass Assembly survey (GAMA, Driver et al. 2011, 2022) and Deep Extragalactic Visible Legacy Survey (DEVILS, Davies et al. 2018, 2021), Thorne et al. (2022a) demonstrated that the SED fitting software PROSPECT (Robotham et al. 2020) accurately disentangles the relative flux contributions of star formation and AGN from the far ultraviolet (FUV) to far infrared (FIR) SED up to $z \approx 5$.

Treating these two critical mechanisms as if they are independent prevents us from better reconciling the union of star formation and AGN activity with the physics of galaxy formation. Especially since feedback from AGN is thought to be an important element that regulates star formation and the baryon cycle in galaxies in the local Universe (e.g., Katsianis et al. 2019; Davies et al. 2022; Wright et al. 2024). The interplay of these processes precipitates a tight relationship between the properties of the SMBH and the surrounding geography of galaxies, such as velocity dispersion of the gas and the mass of the bulge (Magorrian et al. 1998; Gebhardt et al. 2000; Merloni & Heinz 2008; Kormendy & Ho 2013). This connection between star formation and the AGN activity produces a coevolving cosmic star formation history (CSFH) and cosmic AGN bolometric luminosity history (CAGNH) that has persisted for at least 11 Gyr up to the present day (Kauffmann & Haehnelt 2000; Madau & Dickinson 2014; D’Silva et al. 2023c), typifying this tightly knit union of stellar mass assembly and the growth of SMBHs. To further explore these quantities at $z \gtrsim 5$, where much of the current interest

lies, we must turn our attention to high redshift facilities such as the James Webb Space Telescope (JWST, Gardner et al. 2006).

Quantifying how efficiently galaxies form stars and grow their SMBHs at $z \gtrsim 5$ is critical to uncovering the details of the epoch of reionization (EOR) and how the EOR sets the initial conditions for all subsequent galaxy formation and evolution. Before JWST, observations of the UV luminosity function down to $M_{UV} = -13$ at $z \approx 2 - 9$ (Bouwens et al. 2015; Oesch et al. 2018; Stefanon et al. 2021; Bouwens et al. 2021) favored a paradigm where star formation was the dominant source of ionizing photons. However, recent JWST results have renewed interest in the AGN contribution to reionization, with AGN now claiming a higher ionizing emissivity, up to $\approx 50\%$ of what star-forming galaxies contribute, (Harikane et al. 2023) compared to pre-JWST results ($\approx 10\%$, Matsuoka et al. 2018).

Indeed, a striking finding from JWST after roughly 1000 days in space is its reported evidence that AGN activity is widespread at $z \gtrsim 5$, as inferred from detections of broad $H\alpha$ line components ($\gtrsim 1000 \text{ km s}^{-1}$). (Schneider et al. 2023; Matthee et al. 2024; Kocevski et al. 2023; Juodžbalis et al. 2023; Harikane et al. 2023; Larson et al. 2023). AGN activity as it appears in little red dots (LRDs) (Matthee et al. 2024; Kocevski et al. 2024) are especially prevalent, indicating ≈ 1 dex more SMBH accretion per unit comoving volume at $z \approx 4 - 5$ than we would have expected from simply extrapolating the X-ray luminosity function (Akins et al. 2024; Yang et al. 2023). At the same time, JWST results indicate rapid stellar mass assembly at $z \gtrsim 5$ (e.g. Harikane et al. 2023, 2024; Adams et al. 2024; Donnan et al. 2024; Behroozi et al. 2013; Harikane et al. 2022; Lovell et al. 2023), producing $\approx 10^{11} M_{\odot}$ galaxies (e.g., Labbé et al. 2023; Glazebrook et al. 2024) only a few 100 Myr after the Big Bang.

While broad, $\gtrsim 1000 \text{ km s}^{-1}$, $H\alpha$ components as detected by NIRSpec seem to be effective in detecting AGN activity at $z \approx 5$ (e.g., Harikane et al. 2023; Larson et al. 2023; Maiolino et al. 2023), it is unfeasible to obtain high signal to noise spectra for a representative sample of galaxies. As such, in this work we leverage broadband, $\approx 0.2 \rightarrow 4.4 \mu\text{m}$ SEDs of thousands of $z \gtrsim 5$ galaxies as observed by both HST and JWST. We follow the approach of Thorne et al. (2021, 2022a) and use PROSPECT to obtain the astrophysical parameters, M_{\star} , SFR and L_{AGN} , from the SEDs of galaxies between $z = 5.5 - 13.5$. Using those quantities we calculate the stellar mass distribution function (SMF), the star formation rate distribution function (SFRF) and the AGN luminosity distribution function (AGNLF). Stel-

lar mass assembly and the growth of SMBHs are explored from the perspectives of the cosmic stellar mass history (CSMH), CSFH and CAGNH, expanding on the analysis of D’Silva et al. (2023c) who explored the same quantities from $z \approx 0 - 5$. Hence, we directly map the union of star formation and the growth of SMBHs in a self-consistent manner from the EOR through to the local Universe.

In Section 2, we describe the JWST imaging data and our novel processing methods. In Section 3, we describe our multiband photometry and extraction pipeline. In Section 4, we detail our SED fitting methods and our $z \geq 5.5$ sample. In Section 5, we present our key results on the CSFH and CAGNH. In Section 6 we discuss caveats and future work. Finally, In Section 7, we present a summary and concluding remarks. We use standard concordance Λ CDM cosmology with $H_0 = 70 \text{ km s}^{-1} \text{ Mpc}^{-1}$, $\Omega_\Lambda = 0.7$ and $\Omega_M = 0.3$. We use the AB magnitude system Oke & Gunn (1983) and the Chabrier (2003) initial mass function (IMF). Throughout this text, we denote the uniform distribution as $U(a, b)$ and the normal distribution as $\mathcal{N}(\mu, \sigma^2)$.

2. IMAGING DATA

In this paper we used both proprietary and publicly available HST and JWST data. All of our JWST fields were processed with the novel package: JUMPROPE, which stands for the JWST UWA Multiwavelength ProTools Processing Endeavour¹. While JUMPROPE and its many processing steps have been introduced previously (D’Silva et al. 2023a; Windhorst et al. 2023; Robotham et al. 2023), we here provide a complete description of the processing package for reference.

2.1. Query and calibration

UNCAL files, the rawest form of JWST data with which the typical scientist interacts, were downloaded from the Mikulski Archive for Space Telescopes (MAST). JUMPROPE includes this functionality by means of the `astroquery` module, enabling automatic querying of MAST.

After downloading this data, the STScI developed JWST Calibration Pipeline was used to process UNCAL files to CAL. It is this step where, for example, cosmic ray impacts are flagged, sky dark and flat fields are removed and the World Coordinate System (WCS) is applied. In this step, the user must specify the JWST Calibration Reference Data System (CRDS) denomination (e.g., the reference file pmap). Our reductions used five different

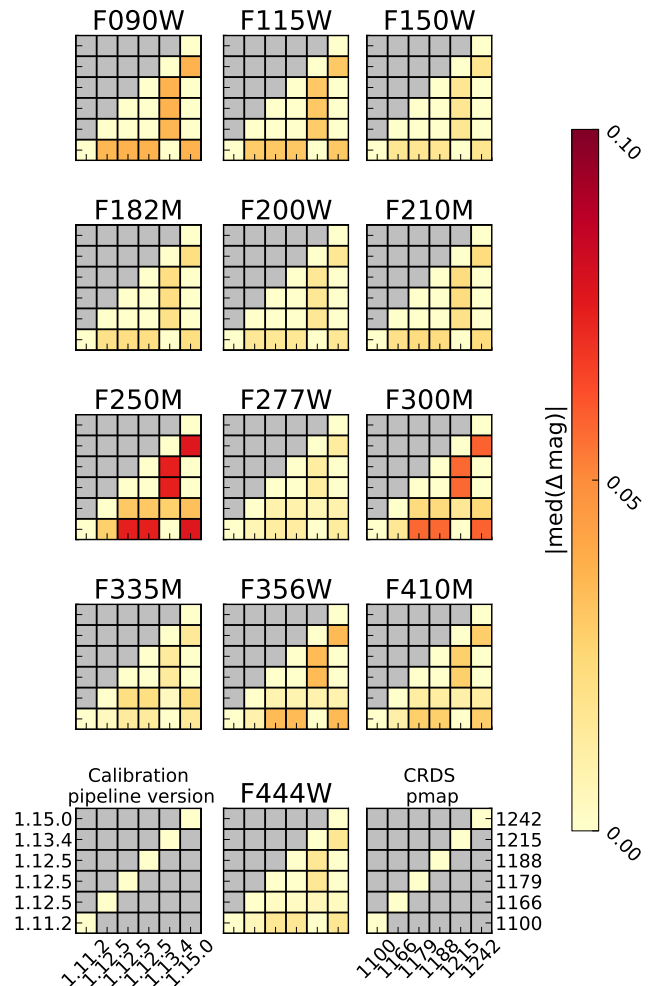


Figure 1. Corner plots of the absolute median magnitude differences of each pixel between calibration pipeline versions and CRDS pmaps per filter. This was computed for the CAL returned from the calibration pipeline.

CRDS pmap and calibration pipeline version combinations because of the frequency of data ingest, but at a minimum used pmap=1100 and pipeline version 1.11.2.

Figure 1 shows the absolute median magnitude difference per pixel between each permutation of the calibration pipeline version and CRDS pmap per filter. These runs were performed on data from programs 1210 and 3215 in GOODS-South over all modules (A and B) and sub-modules (1 \rightarrow 4 for the short wavelength channel) of NIRCcam. For the data used in this work, the most out-of-date combination is calibration pipeline version=1.11.2, pmap=1100 and the most up-to-date is calibration pipeline version=1.13.4, pmap=1215. We also show the results for calibration pipeline version=1.15.0, pmap=1242 which is the most modern combination as of July 2024. The largest difference is ≈ 0.1 mag in the

¹ <https://github.com/JordanDSilva/JUMPROPE>

F250M, but overall the differences are mostly negligible and we used the original pmaps applied to each data set.

2.2. Additional artefact removal

Having produced CAL files, the JWST Calibration Pipeline can then make mosaics using ASTRODRIZZLE. However, at this stage, we intercept the data and perform three crucial processing steps not present in the default pipeline to significantly improve the quality of the data.

2.2.1. $1/f$ removal

Because the NIRCcam detectors export data along read-out lines, variations in the amplifiers can cause banding structures, known as $1/f$ noise, in the images that can compromise the photometry. To correct this, we employed PROFOUND (Robotham et al. 2018) to compute clipped column and row-wise medians on the individual detectors, producing a spatial map of the $1/f$ pattern that was then subtracted from the images. Because the presence of real astronomical sources may bias the row and column medians, the $1/f$ correction has three levels of aggressiveness depending on how crowded the image is. As we produced mostly blank fields, we used the strongest $1/f$ removal. Weaker versions of the $1/f$ algorithm are most appropriate for images of galaxy clusters (e.g., Frye et al. 2023) or in nearby objects with large projected angular sizes that fill the frame (e.g., Keel et al. 2023) where they would otherwise be over-subtracted.

2.2.2. Wisp removal

Wisps are diffuse artifacts in NIRCcam images caused by stray light from bright stars, outside the field of view. Often, the wisps are constrained to fixed locations on the detectors. However, slight variations in the wisp positions due to the exact optical path of the stray photons limits the effectiveness of subtracting pre-determined wisp templates (though this situation will likely improve as JWST continues to build on its existing dataset). Fortunately, the geometry of the NIRCcam detector layout means that the long-wavelength channels are virtually unaffected by the wisps. As such, a special algorithm was developed to remove the wisps (Robotham et al. 2023) that we employed on the data in this work. In essence, the unaffected long wavelength channel is used to isolate the wisp. The algorithm first produces a deep mosaic of the longest wavelength image that overlaps with the affected short channels to encapsulate most, if not all, genuine astronomical sources. The long channel is then appropriately scaled to match the pixel values of the short channel filters as closely as possible. Because the average SED of astronomical objects ensures that

real sources will most likely be detected in at least the long, red filters, the residual when the long is subtracted from the short will be the wisp pattern. The wisp pattern can then be subtracted from the affected image. We note that the presence of wisps affects the $1/f$ removal as the pattern can bias the column and row-wise subtraction, meaning that the wisp removal must be performed before the $1/f$ removal for the short wavelength channels.

2.2.3. Sky removal

Finally, we performed sky subtraction. Again, we used PROFOUND to detect sources and compute sky maps from the largely artifact-free CAL files. The sky maps were then stacked to compute super skies for each module and filter combination, allowing us to constrain global detector properties. For the short wavelength channel, each module of NIRCcam is made of a further four sub-modules, and so we also subtracted a global pedestal value to ensure smooth pixel distributions over the entire breadth of the module. The sky subtraction in detail is represented as

$$(SCI - SKY) = SCI - (M \times SKYSUPER + B + P), \quad (1)$$

where SCI is the science extension, SKY is the sky model, M and B are the coefficients of a linear fit to $SKYSUPER$, the super sky, and P is the pedestal value. This sky model is tested against a simple PROFOUND run, where if the latter option provides a better sky solution, as per the global χ^2 for a normally distributed sky, then the simplified PROFOUND sky is instead subtracted.

This pipeline of $1/f$ removal, wisp correction and sky subtraction is used externally by the PEARLS collaboration, and further details of the pipeline steps can be found in Windhorst et al. (2023); Adams et al. (2024); Conselice et al. (2024).

2.3. Mosaicking with PROPANE

Having produced flat and artifact-free CAL files, the next step is to turn them into mosaics using the image stacking software PROPANE (Robotham et al. 2024). The PROFOUND run performed earlier to calculate the sky statistics preserves the RMS maps of the sky that are used for inverse-variance weighted stacking (inVar = skyRMS⁻²). PROPANE also computes a median stack of the input frames that is more resilient to outlier pixels compared to the inverse-variance stack. Outlier pixels in the inverse-variance stack, which are mostly cosmic rays that survived the initial jump detection in the Calibration Pipeline, are filled in with

the equivalent pixels from the median stack. This way, we leveraged the superior depth of the inverse-variance stack while using the median stack to patch most of the remaining cosmetic artifacts. PROPANE also propagates the mosaic of the inverse-variance image that we used for source detection.

We also provided a reference catalogue, obtained from previous reductions of the JWST fields and observations with ground-based telescopes, to ensure astrometric accuracy. We note, that this pipeline is well suited to adapt source catalogs from forthcoming wide-field surveys with instruments like EUCLID and LSST.

2.4. Field selection

In this work we used $\approx 400 \text{ amin}^2$ of JWST NIR-Cam imaging drawn from the Prime Extragalactic Areas of Reionization and Lensing Science (PEARLS, PIs: R. Windhorst & H. Hammel, PIDs: 1176 & 2738) survey (Windhorst et al. 2023), the JWST Advanced Deep Extragalactic Survey (JADES, PIDs: 1180 PI: D. Eisenstein, 1210 PI: N. Luetzgendorf & 3215, PI: D. Eisenstein & R. Maiolino, Eisenstein et al. 2023; Rieke et al. 2023), the Next Generation Deep Extragalactic Exploratory Public (NGDEEP, PID: 2079, PIs: S. Finkelstein, C. Papovich, N. Pirzkal) survey, (Bagley et al. 2024), the Cosmic Evolution Early Release Science (CEERS, PID: 1345, PI: S. Finkelstein, Bagley et al. 2023; Finkelstein et al. 2023) and, finally, the Public Release IMaging for Extragalactic Research (PRIMER, PID:1837, PI: J. Dunlop) survey. Key information for each field per survey is presented in Table 1.

We demanded that each field contained at least 8 putative NIRCcam filters: F090W; F115W; F150W; F200W; F277W; F356W; F410M; F444W; to enable robust SED fitting. This is true for all of our fields except NGDEEP and CEERS where the F090W filter is missing but is made up for with the availability of HST ACS F814W imaging, covering a similar pivot wavelength. The JADES imaging enjoys additional medium band imaging that we to use in our SED fitting.

Because PEARLS also images cluster environments, we only use the off-cluster, parallel imaging of ACT-CL J0102–4915 (El Gordo), MACS J0416.1–2403 (MACS0416), MACS J1149.5+2223 (MACS1149), and PLCK G165.7+67.0 (G165). PHz G191.24+62.04 (G191) is also a PEARLS-Clusters target, however it is a Planck-selected proto-cluster at $z \approx 2$ and so we used the entire footprint. All of these fields were selected for study because they are largely blank fields, ensuring that our galaxy measurements are not overly biased by dense clusters, intra-cluster light or the effects of strong gravitational lensing.

3. SOURCE DETECTION AND MULTIBAND MEASUREMENTS

After the creation of image mosaics, source detection and multiband photometric measurements were pursued. This pipeline is also implemented in JUMPROPE as described here.

3.1. Star masking

The hexagonal mirror segments of JWST produce the unmistakable 6-pointed point spread function (PSF) pattern when observing stars. The presence of diffraction spikes introduces contaminants during source detection. This is especially significant when folding in observations with the HST, where the flux from the JWST diffraction spikes is missing, leading to SEDs that can resemble $z \gtrsim 5$ drop-out galaxies. Often, the strategy to remove diffraction spikes either involves filtering spurious detections in catalog space or manually masking the affected areas of the region before source detection.

JUMPROPE employs a novel method to mask bright stars before source detection. First, The GAIA source catalog was used to isolate the positions of bright stars in each of the stacked images. Only objects in the GAIA catalog with `classprob_dsc_combmod_star` > 0.98 \wedge `phot_bp_rp_excess_factor` < 2.5 were masked to avoid erroneously masking distant, point-source quasars.

To find the extent of the diffraction spike, 6 rays were shot out in the image matrix from the center of the star at angles of $30^\circ, 90^\circ, 150^\circ, 210^\circ, 270^\circ, 330^\circ$ and the radial flux profiles were calculated. This allowed us to fit a 1D Sérsic profile to the diffraction spike, which we assumed was best represented by the ray with the maximum amount of flux, and note the radius from the star’s center at which the flux descends below the local skyRMS value. With the central positions and the radii of each GAIA star, a simplistic PSF mask of ellipses was transplanted onto a blank matrix of the same dimensions as the image and saved. This process was performed on the stacks of each 10 digit visit ID, where the orientation is natively the position angle of the telescope at the time of observation, ensuring that the orientations of the PSF patterns on the image are all the same. Any residual flux is captured by enabling PROFOUND to dilate the star masks until the curve-of-growth criterion of $\lesssim 1\%$ change is satisfied. An example of this star masking algorithm is presented in Figure 2, showing the field of 2MASS J17554042+6551277.

In some cases, the star mask does not fully capture all of the diffraction spike or the stars are too far out of the field of view. The residual diffraction spike artifacts can be removed in catalog space using improbable colors and proximity to heavily deblended groups of segments (we

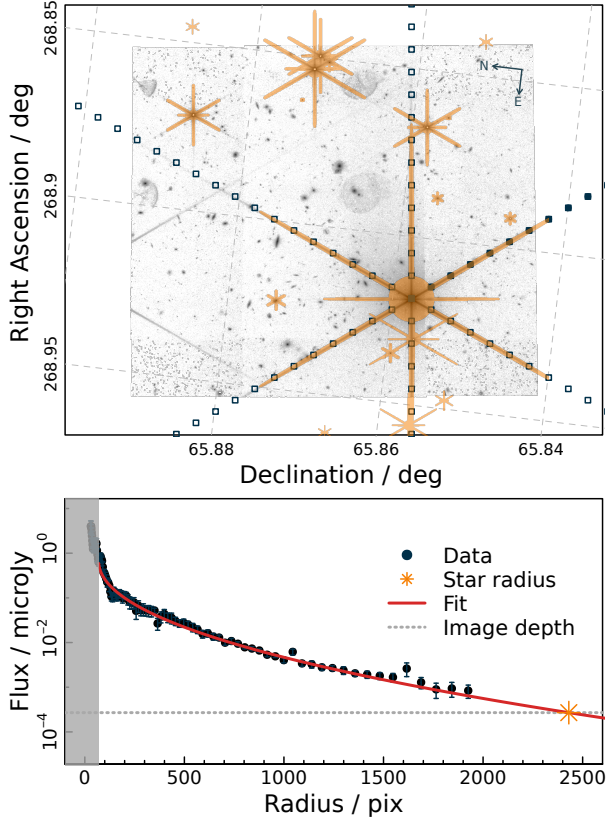


Figure 2. *Top:* Example GAIA star mask of the field containing 2MASS J17554042+6551277 in the F277W filter. The dark blue square points demonstrate the 6 radial rays extended out from the star center. The orange shapes show the extent of the masks pasted on each GAIA star. *Bottom:* The radial flux profile of 2MASS J17554042+6551277 (the brightest star in the field). The solid red line is the 1D Sérsic profile fit. The vertical grey band is the inner pixels that are masked due to being saturated. The horizontal dashed grey line is the approximate local image depth and the orange pointed star is the radius at which the profile descends below the depth.

elaborate further on artifact masking in Section 3.4). To use these masks on the large mosaics, we simply warped the input masks onto the same astrometric grid.

3.2. Photometry with PROFOUND

We used PROFOUND for source detection, optimizing for the faint objects in the images. Only sources that were $\gtrsim 1.5$ times the skyRMS and more than 7 pixels in extent were detected. Four iterations of segment dilations were also enabled to capture the majority of the flux of the objects. Source detection was performed on an inverse-variance-weighted stack of the F277W, F356W and F444W filters. In total, 283,314 objects across all fields were detected with PROFOUND.

The segmentation map was then passed onto each of the images to extract multiband photometry with PROFOUND. An additional phase of dilation was allowed for each image to capture the remaining flux in each band. We measured photometry in both the undilated and dilated segments that were produced by the source detection. Undilated photometry allows for high S/N colors, most appropriate for photometric redshifts, while dilated photometry captures more flux and is thus more appropriate for astrophysical quantities like M_* . The dilated segments conform to the morphology of the galaxies as they appear in the images meaning that we do not need to employ aperture or PSF corrections to obtain an accurate measurement. The flux uncertainties produced by PROFOUND do not account for covariance between pixels that are induced during the mosaicking phase. Blank apertures of various sizes were placed on the images to determine the distribution of sky pixels, capturing the covariance, and the PROFOUND flux uncertainties were appropriately scaled to account for this additional source of noise.

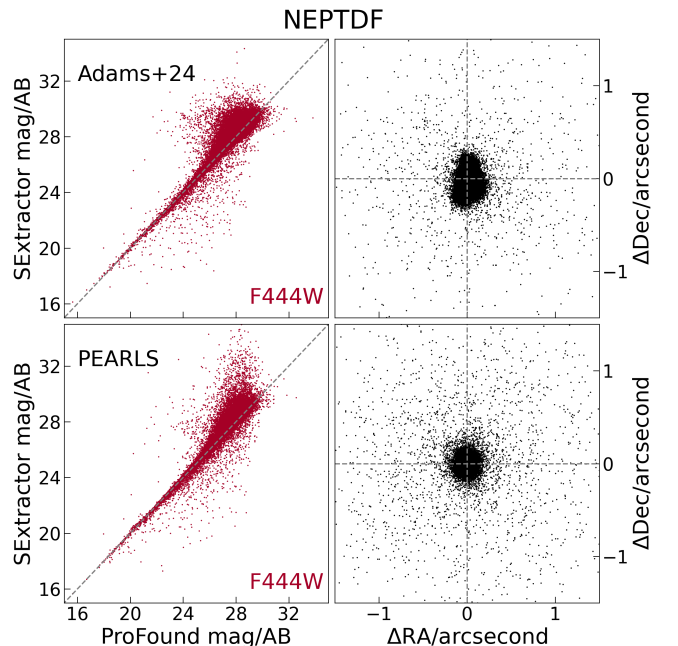


Figure 3. *Left:* F444W PROFOUND photometry against SOURCEEXTRACTOR from the EPOCHS data set (*top*, Conzelice et al. 2024; Adams et al. 2024) and the PEARLS team (*bottom*). *Right:* Astrometry difference between EPOCHS and PEARLS.

To find the detection sensitivities of each of our fields, we placed $0.15''$ apertures onto blank areas of the F277W + F356W + F444W detection images and computed the 5σ limiting magnitudes from the blank sky pixel distribution.

Field	5σ depth/mag	Total area	Effective area/arcmin ²	Right Ascension	Declination
PEARLS El Gordo Parallel	29.36	5.01	4.90	15.74	-49.21
PEARLS G165 Parallel	29.09	5.01	4.92	171.76	42.47
PEARLS MACS0416 Parallel	29.51	14.32	13.84	64.07	-24.07
PEARLS MACS1149 Parallel	29.31	5.026	4.99	177.40	22.35
PEARLS G191	29.27	10.03	9.80	161.16	33.83
PEARLS NEPTDF	29.58	65.10	60.95	260.70	65.82
PEARLS WFC3-ERS	29.37	10.03	9.78	53.18	-27.70
JADES GOODS-S	30.46	26.77	26.23	53.16	-27.79
JADES Origin GOODS-S	30.43	9.33	9.05	53.06	-27.87
NGDEEP GOODS-S	29.81	10.90	10.27	53.25	-27.84
CEERS Extended Groth Strip	29.06	102.43	99.50	214.91	52.87
PRIMER COSMOS	28.93	145.47	138.38	150.13	2.33

Table 1. 5σ magnitude depths in $0.15''$ apertures and area in arcmin² covered by our fields. The effective area is the area remaining after masking. The right ascension and declination are the J2000 central coordinates of the fields in degrees.

Table 1 shows the 5σ limiting magnitudes in the F277W + F356W + F444W detection image for our fields and the area covered.

Figure 3 shows a comparison between our PROFOUND photometry in the NEPTDF and SOURCEEXTRACTOR photometry from the EPOCHS data set (Conselice et al. 2024; Adams et al. 2024) and the PEARLS collaboration (Cohen, S priv. comm.). The comparison data sets used ASTRODRIZZLE to produce the mosaics, as opposed to PROPANE. A key result is the propensity for PROFOUND to obtain $\approx 10\%$ more flux, especially at $\text{mag} \gtrsim 26$, compared to SOURCEEXTRACTOR on account of its segment dilation logic. Though only the F444W photometry is shown in this figure, similar trends are exhibited in all other filters. We also see that astrometric differences are $\lesssim 1''$. Overall, the systematic differences between ASTRODRIZZLE/SOURCEEXTRACTOR photometry and ours are minimal and as expected.

3.3. Folding in HST observations

HST observations were included to further sample the $\lambda < 0.9 \mu\text{m}$ part of the observed galaxy SEDs. This was possible for all fields except the parallel fields of G165, G191, and El Gordo. Unsurprisingly, the vast majority of HST observations, such as from the Hubble Frontier Fields (Lotz et al. 2017), targeted the main cluster in those cases.

For PRIMER, CEERS, NGDEEP and JADES we used ACS/WFC F606W and F814W data from the CANDELS HST program (Koekemoer et al. 2011; Grogin et al. 2011), warping the images to the JWST astrometric grid and using the magnitude zero-points as reported by the CANDELS repository². For the

NEPTDF we used ACS/WFC F435W and F606W data from HST programs GO 15278 and GO 16252/16793 (O’Brien et al. 2024). For the WFC3-ERS field we used WFC3/UVIS F225W, F275W, F336W data from the HST Early Release Science programs 11359 (Windhorst et al. 2011). These data were obtained from the PEARLS collaboration and we used their reported magnitude zero-points.

The HST data were generated using ASTRODRIZZLE as opposed to PROPANE, but the difference between the two codes is negligible (Robotham et al. 2024).

3.4. Artefact flagging

While the PROFOUND detection was tuned to minimize the incidence of false-positive sources, we imposed further selections in the catalog to reject as many resilient artifacts as possible.

Hot pixels caused by cosmic ray impacts were rejected if the effective radii of sources were below the approximate angular resolution of NIRCcam at $2.7 \mu\text{m}$ ($\approx 0.11''$), more than a quarter of the total flux was in the central pixel and $S/N > 5$. The motivation for this is that energetic cosmic rays strike the detector without passing through the optics and deposit their energy into basically a single pixel of the CCD.

Stars, not in the GAIA catalogue, were flagged if the sources inhabited the stellar locus in the plane of detected magnitude versus effective radius and in the plane of the F150W versus F277W-F444W color. In both cases the stellar locus was identified by fitting kernel density estimations in bins of magnitude and identifying the minimum between the distributions. A similar strategy, using these planes to discern stars from genuine galaxies, was used by Bellstedt et al. (2020a); Windhorst et al. (2023) and will be used for galaxy number counts as part of the SKYSURF project (Tompkins in prep.).

² <https://archive.STScI.edu/hlsp/candels>

Residual diffraction spikes were flagged if sources inhabited the stellar locus in the plane of the F150W versus F277W-F444W color and were near to bright groups. The motivation for this selection is that the diffraction spikes that survive the initial star masking will be highly fragmented because of the substructure in the NIRCcam PSF and exhibit stellar colors.

Only sources with `edge_excess` ≤ 1 and `edge_frac` > 0.5 , which are measurements reported by PROFOUND, were included in the subsequent analysis of this paper. `Edge_excess` is defined as the ratio of segment edge pixels to the expected number given the elliptical geometry measurements of the galaxy, and a value ≥ 1 is likely indicative of compromised photometry. `Edge_frac` is the fraction of segment edge pixels that are touching the sky, and so we required at least 50% of pixels to be touching the sky to limit sources with many boundary neighbours and/or over-fragmented.

3.5. Milky Way extinction correction

In addition to the *in-situ* dust screen of the extragalactic sources, dust in the Milky Way is an additional source of attenuation. To obtain rest-frame fluxes of the sources, Milky Way attenuation must therefore be corrected.

$E(B - V)$ values from the Planck Collaboration et al. (2013) all-sky map of microwave dust haze were combined with the Fitzpatrick & Massa (2007) extinction curve and $R_V = 3.1$ to compute the attenuation value: $A(\lambda) > 0$. The observed magnitudes, and likewise fluxes, were then corrected as

$$\text{mag}_{\text{emit}}(\lambda) = \text{mag}_{\text{observed}}(\lambda) - A(\lambda). \quad (2)$$

4. SED FITTING

The SED is a record of the astrophysical processes that have occurred. Using SED fitting, we extracted the photometric redshift (z_{phot}), M_{\star} , SFR averaged over 10 Myr and L_{AGN} . A two phased approach of first fitting z_{phot} and then M_{\star} , SFR and L_{AGN} was employed to reduce degeneracies of the astrophysical parameters with distance.

4.1. Photometric redshifts with EAZY

The z_{phot} was initially fitted with the widely used EAZY package (Brammer et al. 2008). No prior was assumed and absorption from the IGM was enabled. The undilated color photometry was used in this initial phase of z_{phot} fitting.

We used the standard template set included in EAZY, derived from the Flexible Stellar Population Synthesis code (Conroy & Gunn 2010), supplemented with updated templates from Larson et al. (2023). The updated

templates include model SEDs with bluer UV colors that were found to be more representative for simulated $z \gtrsim 7$ galaxies than the standard EAZY templates. EAZY makes an SED model of linear combinations of templates and uses least-squares fitting to minimise the residual of that model and the data. As such, the degrees of freedom, dof , for EAZY models is the difference between the number of data points and the number of template combinations.

With a limited number of filters, spectral features, such as the Lyman break at $\lambda \approx 0.1216 \mu\text{m}$ and the Balmer break at $\lambda \approx 0.3645 \mu\text{m}$ in the rest-frame, are sparsely sampled meaning that confusion can arise in the fitting and lead to a distribution of possible z_{phot} solutions. As such, striving to discern genuine $z \gtrsim 5$ galaxies, we used the following selection:

- $\int_5^{25} P(z_{\text{phot}}) dz \geq 0.8$ to ensure a robust probability of the high redshift solution.
- $S/N_{\text{Ly}\alpha} < 2\sigma$, where $S/N_{\text{Ly}\alpha}$ is the combined signal-to-noise for fluxes blueward of the Lyman break to ensure significant absorption of Lyman continuum flux as expected given the z_{phot} .
- EAZY_{highz} must be better fit than EAZY_{lowz} as per the χ^2 test at the 2σ level.

For the last item of the selection, EAZY_{highz} refers to one EAZY fit where $z_{\text{phot}} \in [0.01, 24.99]$ and EAZY_{lowz} is where $z_{\text{phot}} \in [0.01, 4.5]$. The use of two EAZY runs in this manner allowed us to better visualise the low z_{phot} solution. The critical value of $z_{\text{phot}} = 4.5$ was chosen as a buffer range to compute M_{\star} , SFR and L_{AGN} distributions at $z_{\text{phot}} \geq 5.5$.

We used the χ^2 distribution to omit poor fits to the data and to discern between EAZY runs. We accepted $z_{\text{phot}} \geq 4.5$ provided EAZY_{highz} better represented the data compared to EAZY_{lowz} with 2σ significance.

If this test showed that both runs represented the data similarly, we considered the $dof = N_{\text{templates}} - N_{\text{fluxes}}$ of the two runs and used the χ^2 distribution to test whether the model with higher dof provided a justifiably better fit than the model with lower dof . In this case, we accepted $z_{\text{phot}} \geq 4.5$ provided that the dof for EAZY_{highz} was greater than that of EAZY_{lowz} and that we could justify the use of the more complex model with 2σ significance. When both runs had the same dof , then there is no statistical difference and we did not subsume that source into our $z_{\text{phot}} \geq 4.5$ sample.

Figure 4 shows some of the z_{phot} against confirmed z_{spec} in the CEERS and JADES Goods-South fields, as determined by performing a coordinate match with an accuracy of $1''$. CEERS and JADES are the two

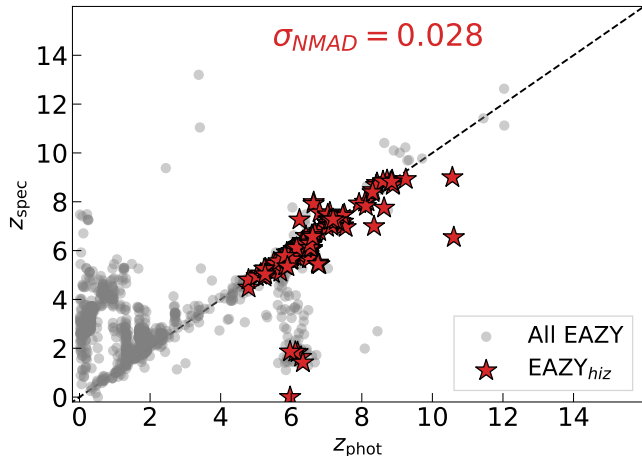


Figure 4. z_{spec} against z_{phot} from the CEERS Extended Groth Strip and JADES GOODS-South programs. Grey points are all EAZY_{hiz} z_{phot} . Red points are only the sources that survived the $z_{\text{phot}} > 4.5$ selection. The dashed, grey line is the equality line.

greatest repositories of spectroscopic redshifts to date (Arrabal Haro et al. 2023; Nakajima et al. 2023; Bunker et al. 2024). Overall, we exhibit reasonable agreement against the spectroscopic results. The z_{phot} outliers, in grey, are most likely caused by a combination of confusion of the Lyman and Balmer breaks as per the EAZY templates, complicating the redshift extraction. The agreement further improves when only the sources that pass the aforementioned $z_{\text{phot}} \geq 4.5$ selection are included, as evidenced by the low $\sigma_{\text{NMAD}} = 0.028$. The agreement is quantified using the normalised-median-absolute-deviation:

$$\sigma_{\text{NMAD}} = 1.48 \times \text{med} \left(\left| \frac{\Delta z - \text{med}(\Delta z)}{1 + z_{\text{spec}}} \right| \right), \quad (3)$$

where $\Delta z = z_{\text{phot}} - z_{\text{spec}}$. In total, 4585 $z_{\text{phot}} > 4.5$ candidates were obtained with this selection.

Interestingly, a few $z_{\text{spec}} \gtrsim 10$ sources did not survive our photometric selection, meaning that we could not, with at least 2σ confidence, rule out those sources as lower redshift interlopers, as per their z_{phot} , with this strategy. In most of these cases, both the z_{phot} and z_{spec} are informed by the Lyman break, and since this is only a single spectral feature we could not significantly separate the EAZY_{lowz} and EAZY_{hiz} solutions. Where possible, we subsumed the z_{spec} into our sample and adopted a normal $P(z)$ centred on z_{spec} and $\sigma = 0.028$ for the sake of SED fitting with PROSPECT. Note, only $\approx 5\%$ of the entire sample have secure z_{spec} and are thus not expected to introduce a significant bias in the results.

4.2. PROSPECT

Having generated $P(z)$'s for our sample, we then used the SED fitting software PROSPECT to determine the astrophysical parameters of interest: M_* , SFR, L_{AGN} . We ran PROSPECT on our sample of $z_{\text{phot}} \geq 4.5$ candidates, using the total fluxes. A brief description of PROSPECT is given here:

1. Star formation history (SFH). PROSPECT models the SFHs of galaxies parametrically with flexible, four-parameter models, which are essentially skewed normal distributions (see equations 1-5 in D'Silva et al. 2023c). While this cannot reproduce stochasticity in the true SFH, it has been shown that the SFH parametrisation in PROSPECT reproduces the average behavior of galaxy SFHs (Robotham et al. 2020). As such, the true power of PROSPECT is derived from its application to large samples as presented here. The SFH is then combined with the Chabrier (2003) IMF and Bruzual & Charlot (2003) stellar spectral libraries to test SEDs against the data in the generative model.
2. Metallicity history (ZH). A key aspect of PROSPECT is its flexible metallicity evolution linearly tied to the SFH. The motivation for this is to adequately capture the physics of chemical enrichment as a result of stellar evolution. Bellstedt et al. (2020b) found that the metallicity evolution was crucial to reproduce the expected peak of CSFH at $z \approx 1.5 - 2$.
3. AGN. PROSPECT employs the Fritz et al. (2006) description to model the AGN component. Here, the SED of the primary source is assumed to be a combination of power laws. The torus is assumed to be a flared disk of a range of dust grain sizes and with a smooth spatial distribution. A free parameter of the Fritz et al. (2006) model is the optical depth of the torus, which is needed to explain how the primary source is attenuated. Of use in this work is the bolometric luminosity of the AGN, L_{AGN} , which is a free parameter in the Fritz et al. (2006) model.
4. Attenuation and reemission. PROSPECT uses the Charlot & Fall (2000) model to describe attenuation by dust. Here, stellar light can be attenuated by both the interstellar dust screen spread throughout the galaxy and the dust enshrouded birth clouds of the stellar nurseries. Physically, the attenuated light is then reemitted in the IR and beyond, and this is prescribed in PROSPECT with the Dale et al. (2014) reemission model. Note, however, that we cannot constrain the dust emission due

to our photometry not probing wavelengths longer than the rest-frame optical at $z \gtrsim 5$. We therefore fixed the parameters $\alpha_{SF} = 1$ and $\alpha_{BC} = 3$, essentially fixing the dust temperature and the wavelength of the peak of the dust emission. We also invoked priors for the optical depths of the dust screen and birth clouds of the form:

$$-20 \times \text{erf}(\log_{10}(\tau_{\text{screen}}) - 2), \quad (4)$$

$$\log_{10}(\tau_{\text{birth}}) \sim \mathcal{N}(-0.2, 0.5^2), \quad (5)$$

which is the same as the set-up used in [Thorne et al. \(2021\)](#).

5. Photometric redshift. Because PROSPECT is a fully generative SED model, directly fitting z_{phot} with PROSPECT mitigates template incompleteness that may be present in EAZY, allowing us to further refine the z_{phot} . We modified PROSPECT to make it more appropriate for photometric redshift fitting, essentially tying the maximum age of stars to the age of the Universe at the test z_{phot} . The original design of PROSPECT was to ingest z_{spec} , where this would not have been an issue. The $P(z)$ of each source obtained from EAZY was used as a prior on z_{phot} , ensuring that the desired astrophysical parameters have realistic uncertainties (e.g., [Acquaviva et al. 2015](#)). The IGM absorption is implemented as a function of redshift as a cumulative normal distribution³ with mean= 3.8 and standard deviation= 1.2, such that the IGM is totally ionized by $z \approx 6$ and all flux blue-ward of the Lyman break is absorbed and reemitted as emission lines.

In conjunction with PROSPECT, the optimisation software HIGHLANDER was used to sample the multimodal posterior distributions. HIGHLANDER switches between a genetic algorithm and Markov-Chain-Monte-Carlo (MCMC) to traverse local extrema and identify the global maximum (e.g., [Thorne et al. 2021](#)). This allowed us to refine the z_{phot} even in the presence of the EAZY $P(z)$ because, as we further elaborate on in Section 4.4, the PROSPECT z_{phot} is not necessarily at the maximum likelihood EAZY z_{phot} .

Correctly disentangling of the light contributions from stars and from AGN is essential when we wish to study these two processes in unison. As such, we performed two PROSPECT runs, with and without an AGN component. Throughout the text, the two runs are referred

to as $\text{Pro}_{\text{Stellar+AGN}}$ and $\text{Pro}_{\text{Stellar}}$. Other than the inclusion of the AGN model, the set up between the two runs was identical.

Because $\text{Pro}_{\text{Stellar+AGN}}$ introduces more free parameters, we used the Bayesian Information Criterion (BIC) to judge whether the extra complexity justifiably improves the SED fit. The BIC is an approximation for the marginal likelihood, or model evidence, and calculated as

$$BIC = kN - 2LP, \quad (6)$$

where k is the number of free parameters, N is the number of photometric points and LP is the value of the log posterior distribution at the maximum-a-posteriori solution of parameters. The BIC penalises the extra free parameters in $\text{Pro}_{\text{Stellar+AGN}}$, and we accepted the model with the lower BIC.

In cases where the $\text{Pro}_{\text{Stellar}}$ was preferred, we considered two extremes of the L_{AGN} to effectively bound the possible AGN contribution. The lower limit ($L_{\text{AGN}}^{\text{lo lim}}$) was set such that $L_{\text{AGN}} = 0$. The upper limit ($L_{\text{AGN}}^{\text{up lim}}$) was set by finding the L_{AGN} for an unobscured AGN template from the [Fritz et al. \(2006\)](#) models that contributed no more than 20% of the flux in the summed F277W+F356W+F444W $\text{Pro}_{\text{Stellar}}$ SED model fluxes. We note that SED contributions from AGN above 10% usually identified with significant AGN (e.g., [Thorne et al. 2022b](#)); we doubled the threshold in this work because we also assumed a 10% uncertainty floor on the flux measurements that went into the SED fitting. This meant that we could constrain a realistic bound of possible AGN contribution to the galaxy SEDs where the true AGN contribution must lie somewhere in between. We may miss AGN activity with the data at hand for those galaxies that preferred the $\text{Pro}_{\text{Stellar}}$ fit because we do not probe redder wavelengths to uncover a faint AGN component.

Figure 5 shows SED fits to a compilation of noteworthy sources including Maisie’s Galaxy at $z_{\text{spec}} = 11.4$ ([Finkelstein et al. 2022](#)), a LRD in the COSMOS field ([Kocevski et al. 2024](#)) and a $z_{\text{phot}} \approx 13$ galaxy from the NEP-TDF.

4.3. Vetting brown dwarf contaminants

Absorption features of brown dwarf stars in the Milky Way can mimic similar spectral features of $z \geq 3$ galaxies hosting AGN ([Langeroodi & Hjorth 2023](#)). We employed the Sonora Bobcat models ([Marley et al. 2021](#)) to test whether the SEDs were better fit by galaxy or brown dwarf SEDs.

To compare like-for-like in this case, the LP term in Equation 6 was replaced with an effective likelihood given by

³ The R function is `pnorm(z, 3.8, 1.2)`

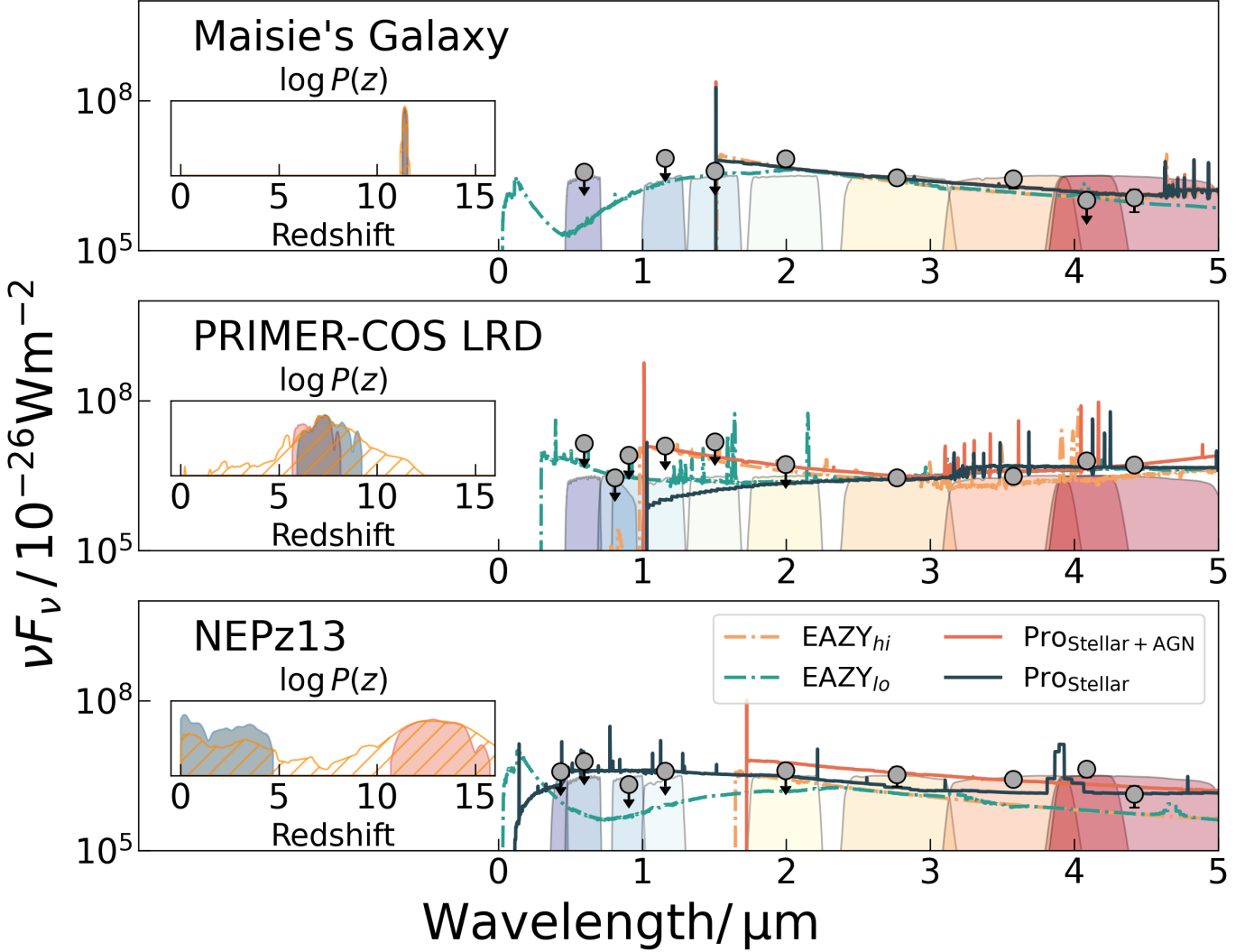


Figure 5. Select SEDs of noteworthy sources. In all panels, the grey points with error bars are our photometry. 2σ upper limits are noted with arrows. The dot-dashed orange line is the EAZY_{hiz} SED fit at the *maximum-a-posteriori* location (and peak of the $P(z)$ as such), while the dot-dashed green line is the EAZY_{lowz} SED fit. The solid orange line is the ProStellar+AGN SED fit while the solid blue line is the ProStellar SED fit. The HST and JWST filter transmission curves are shown with rainbow colors. Each panel is inset with the $\log(P(z))$ from EAZY_{hiz}, ProStellar+AGN and ProStellar, with a similar color scheme as the SED lines. *Top:* SED of Maisie’s Galaxy at $z_{\text{spec}} = 11.4$ (Finkelstein et al. 2022). *Middle:* SED of one of the LRDs in the COSMOS field (Kocevski et al. 2024). *Bottom:* SED of a $z_{\text{phot}} \approx 13$ galaxy from the NEP-TDF.

$$LL_{\text{eff}} = \sum^{\text{NIRCam}} \log \left[\frac{1}{\sigma_i \sqrt{2\pi}} \exp \left(-\frac{(F_i^{\text{obs}} - F_i^{\text{model}})^2}{2\sigma_i^2} \right) \right], \quad (7)$$

where F_i^{obs} and σ_i are the observed fluxes and errors, F_i^{model} are the model fluxes from the best fit, maximum-a-posteriori, SED and the summation runs over all NIR-Cam filters. As such, sources were considered brown dwarfs when the Sonora template was preferred as per the lower BIC to both the ProStellar and ProStellar+AGN runs. In total, 44 out of the 4585 $z_{\text{phot}} \gtrsim 4.5$ candidates were identified as brown dwarfs.

4.4. Final sample

Interestingly, 594 galaxies with $z_{\text{phot}} \geq 4.5$ as identified by EAZY ended up with lower z_{phot} when fitted with PROSPECT, even when passing in the EAZY $P(z)$. A potential reason for this may be template incompleteness as the generative model in PROSPECT allows for more flexibility in the model SEDs to compare against the data in contrast to the 18 SED templates used in EAZY.

Figure 6 shows an example SED of a galaxy in the JADES field where the z_{phot} determined from PROSPECT did not agree with the initial $z_{\text{phot}} \geq 4.5$ determination from EAZY. Comparing the $P(z)$ ’s, it can

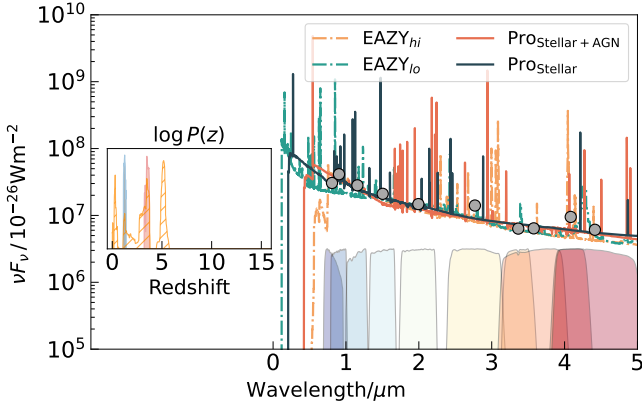


Figure 6. SED of galaxy 101396 from the JADES field in our photometric catalogue. The grey points with error bars show the photometry. The dot-dashed orange line is the EAZY_{hiz} SED fit while the dot-dashed green line is the EAZY_{lowz} SED fit. The solid orange line is the PROStellar+AGN SED fit while the solid blue line is the PROStellar SED fit. The HST and JWST filter transmission curves are shown with rainbow colors. The inset panel is the $\log(P(z))$ from EAZY_{hiz}, PROStellar+AGN and PROStellar, with a similar color scheme as the SED lines.

be seen that the increased flexibility with PROSPECT prefers the local maxima from the EAZY $P(z)$, in contrast to the global maximum at $z_{\text{phot}} \approx 5.0$.

In the subsequent analyses of this paper, we consider the robust sample of 3947, being the galaxies whose $z_{\text{phot}} > 4.5$ survived the two phased filtration through EAZY and PROSPECT.

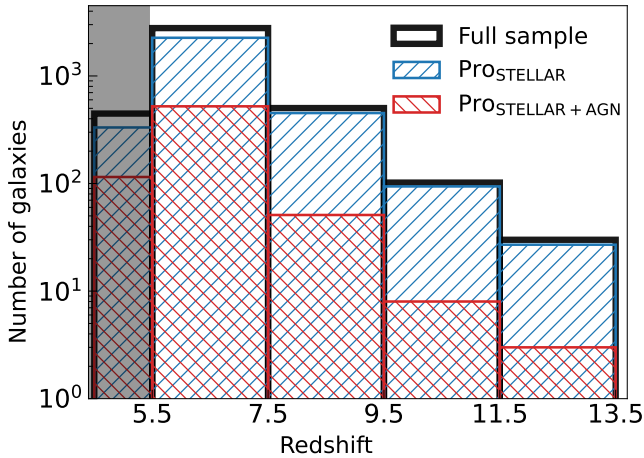


Figure 7. Redshift distribution of 3947 galaxies. The black histogram is the distribution for the entire sample. The blue hatched histogram is the distribution for the subset of the sample better fit with PROStellar, while the red hatched histogram is the same for PROStellar+AGN. The grey band is the redshift buffer range of $z_{\text{phot}} = 4.5 - 5.5$ used when deciding between EAZY_{lowz} and EAZY_{hiz}.

Figure 7 shows the redshift distribution of the final sample.

5. RESULTS

With the final sample of redshifts and astrophysical quantities, we explored the interface of stellar mass assembly and SMBH growth in four bins of redshift from $z = 5.5$ to $z = 13.5$. The upper edge of $z = 13.5$ was chosen because extreme emission line galaxies at $z \approx 4 - 5$ can mimic the colors of $z \gtrsim 13.5$ galaxies, introducing a pathological source of systematic uncertainty in constraining the redshift from photometry alone (Zavala et al. 2023; Arrabal Haro et al. 2023).

5.1. Effective volumes

Due to sensitivity limits of astronomical instruments, inherently faint galaxies will be missed from sample selections. This causes an unphysical turn-over in the histogram toward low luminosities, known as the Malmquist bias. We therefore employed V/V_{max} corrections, aiming to find the maximum redshift, and therefore volume, that the galaxies could inhabit before dropping out of the survey (e.g., Weigel et al. 2016). We used the 5σ limiting magnitudes that we found in Table 1 and redshifted the best fit SED until the average flux in the three detection bands was fainter than the survey limit. If z_{max} exceeded the uppermost edge of the redshift bin in question, then that uppermost edge was instead used to calculate V_{max} .

We also computed a magnitude completeness function to account for the implicit selection imposed by our PROFOUND source finding parameters. In each of our fields a representative 12.25 amin^2 area was chosen where source injection-recovery simulations were performed (e.g., Leethochawalit et al. 2022). The magnitude-completeness is calculated as

$$C(\text{mag}_i) = \frac{N(\text{mag}_{\text{rec},i}) - N(\text{FP}_i)}{N(\text{mag}_{\text{in},i})}, \quad (8)$$

where $C(\text{mag}_i)$ is the completeness value in the i^{th} magnitude bin, $N(\text{mag}_{\text{rec},i})$ is the number of recovered magnitudes, $N(\text{mag}_{\text{in},i})$ is the number of injected magnitudes and $N(\text{FP}_i)$ is the number of false-positives. $N(\text{FP}_i)$ was calculated by performing a coordinate match of the recovered sources against the injected ones and finding those that were unmatched. We used the 2D profile fitting and generation code PROFIT (Robotham et al. 2017) to generate 200 fake sources. The redshift distribution was assumed to be uniform and the distributions for effective radius, axial ratio and Sérsic index were adapted from observations of $z \gtrsim 3$ galaxies observed by JWST (e.g., Kartaltepe et al. 2023; Ferreira

et al. 2023). The exact same PROFOUND set up was then employed to recover the injected sources. This process of source injection and recovery was repeated 50 times to obtain a Monte-Carlo uncertainty on the completeness values, and the completeness curve was fitted with the logistic function (e.g., Leethochawalit et al. 2022).

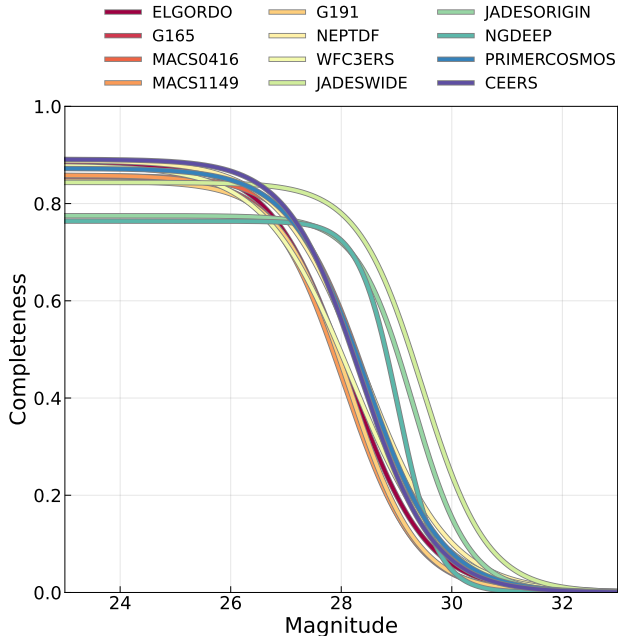


Figure 8. Magnitude completeness for all fields used in this work, as described in the figure legend. Magnitudes are obtained from the combined F277W, F356W and F444W used in the detection image.

Figure 8 shows the magnitude-completeness fitted logistic functions for each of our fields. We hit a maximum of $\approx 80\%$ completeness toward bright magnitudes as those bright galaxies are fragmented in the source detection process. The reader is reminded that the source detection pipeline was optimised to extract the faint sources, where overblending is not an issue. In most fields we are $\approx 50\%$ complete up to 28 mag, except for JADES and NGDEEP that both enjoy superior depth with $\approx 50\%$ completeness up to 29 mag.

The effective volume was then calculated for each galaxy in the final sample as

$$V_{\text{eff}} = V_{\text{max}} \times C(\text{mag}). \quad (9)$$

5.2. Stellar mass, SFR, AGN luminosity completeness

The completeness limit of M_* , SFR, L_{AGN} is necessary when constructing their distribution functions as galaxies exhibit a range of mass-to-light ratios that can introduce biases into the distribution (Weigel et al. 2016). For each galaxy, we computed

$$\log_{10}(M_{\text{lim},i}) = \log_{10}(M_{*,i}) + 0.4 \times (\text{mag}_i - \text{mag}_{\text{lim}}) \quad (10)$$

where $M_{\text{lim},i}$ is the limiting mass for which we could detect the i^{th} galaxy given its observed $M_{*,i}$ and mag_i as per the survey mag_{lim} , presented in Table 1. Then, in each bin of redshift, we calculated the 80th percentile of the limiting masses and for galaxies with greater than 50% magnitude completeness, allowing us to compute a mass completeness limit as a function of redshift. For consistency, a similar calculation was performed for the SFR and L_{AGN} .

5.3. Distribution functions

The census of M_* , SFR, L_{AGN} was obtained by computing essentially the histogram of those quantities per unit comoving volume. In each redshift bin and for each quantity, we fitted a double power law function to the distributions:

$$\phi(x) = \frac{\phi^*}{(x/x^*)^{-\alpha} + (x/x^*)^{-\beta}}, \quad (11)$$

where ϕ^* is a normalization term, α is the slope of the function for $x < x^*$, and β is the slope for $x > x^*$.

Priors were also used to guide the fit, and the same priors used in every redshift bin. A tight prior on the faint-end slope, α , was employed for the SMF and SFRF, being informed by results from the $z \lesssim 5$ Universe (e.g., Thorne et al. 2021).

Solutions where $\alpha \leq -1$ produce divergent measurements for the CSMH/CSFH, under the assumption that the distributions extend monotonically as a power law toward low M_* and SFR (see Equation 12). This situation would be avoided if the SMF/SFRF flattens or turns over at low values. With this data, we do not probe faint enough galaxies to constrain this behavior. However, HST observations of faint galaxies magnified by lensing clusters show that the UV luminosity function at $z \gtrsim 6$ seems to extend as a power law even down to $M_{\text{UV}} \approx -13 \rightarrow -15$ (Atek et al. 2018; Bouwens et al. 2022). With respect to the M_* and SFR, solutions where $\alpha \geq 0$ are suggestive of incompleteness in the domain that we probe with this data.

The double power law was fitted using the Bayesian fitting software DFTOOLS (Obreschkow et al. 2018). DFTOOLS employs bin-free fitting and correct treatment of the Eddington bias as a result of the uncertainties on the quantities. A comparison of the double power law and the Schechter function (Schechter 1976) showed that the double power law was the preferred model to describe the SMF, SFRF and AGNLF as per the posterior

Quantity	$\log_{10}(\Phi^*)$	α	β	$\log_{10}(x^*)$
M_*	$\mathcal{N}(-2.0, 5.0^2)$	$\mathcal{N}(-0.5, 0.1^2)$	$\mathcal{N}(-2.0, 3.0^2)$	$\mathcal{N}(8.5, 1.0^2)$
SFR	$\mathcal{N}(-2.0, 5.0^2)$	$\mathcal{N}(-0.5, 0.1^2)$	$\mathcal{N}(-2.0, 3.0^2)$	$\mathcal{N}(1.0, 1.0^2)$
$L_{\text{AGN}}^{\text{uplim}}$	$\mathcal{N}(-4.0, 5.0^2)$	$\mathcal{N}(-0.5, 0.1^2)$	$\mathcal{N}(-2.0, 1.0^2)$	$\mathcal{N}(45.0, 1.0^2)$

Table 2. Prior distributions used for fitting the double power law functions to the SMF, SFRF and AGNLF. ϕ^* is a normalization term, α is the slope of the function for $x < x^*$, and β is the slope for $x > x^*$

odds reported by DFTOOLS. In general, for all distributions there is excess number density toward large values that could not be adequately encapsulated by the exponential decline of the Schechter function beyond the characteristic knee.

To compute the AGNLF we used the L_{AGN} of the ProStellar+AGN preferred fits as is, whilst we used the $L_{\text{AGN}}^{\text{uplim}}$ from the ProStellar preferred SED fits, as described in Section 4. The AGNLF fit that we here report is thus an upper limit. We could not perform an equivalent fit for the $L_{\text{AGN}}^{\text{loim}}$ for the ProStellar preferred SED fits due to the dearth of data points especially in the highest redshift bin. For those, we instead show the binned quantities. Note, that this situation will improve with increased survey area, to better sample bright L_{AGN} , and redder bands to better constrain fainter L_{AGN} from the SED fitting. We only fit for $L_{\text{AGN}} < 10^{46} \text{ erg s}^{-1}$ due to an upturn in the number densities, especially in the lowest redshift bin where many of those objects are LRDs and may have unphysical L_{AGN} (we elaborate on this in Section 6.2). Including all L_{AGN} values does not significantly change the double power law fits.

Figure 9 shows the fitted distributions. For comparison, we also calculated the $1/V_{\text{max}}$ distributions in bins of 0.5 dex. Overall, our results exhibit broad agreement in comparison to previous measurements in the literature. We wish to highlight that these astrophysical quantities have been inferred simultaneously with PROSPECT, and that we have endeavored to obtain a representative census of M_* , SFR and L_{AGN} . Subtle departures are most likely attributed to differences in methodologies as elucidated below.

The SMFs from Song et al. (2016) were determined by convolving the UV luminosity function from Finkelstein et al. (2015) with the $M_{\text{UV}} - M_*$. On the other hand, Stefanon et al. (2021) compute the SMF, but the calculation of M_* is not always from full SED fitting, especially for the galaxies without a significant Spitzer/IRAC detection (e.g., their Fig. 4). The SMFs from Navarro-Carrera et al. (2024); Harvey et al. (2024) are most appropriate comparison data sets as they use JWST photometry; although, they used different SED fitting codes.

All of the SFRFs against which we compare (Bouwens et al. 2015, 2023; Harikane et al. 2023; Adams et al.

2024) were converted from computed UV luminosity functions as $\text{SFR} = 0.63 \times 1.28 \times 10^{-28} \times L_{\text{UV}}$, where L_{UV} is the UV luminosity at 1500 \AA in units of $\text{erg s}^{-1} \text{ Hz}^{-1}$ and the factor of 0.63 is the relevant conversion of a Salpeter to Chabrier IMF (Madau & Dickinson 2014). This L_{UV} to SFR conversion is a function of at least metallicity and the shape of the SFH, and is therefore a potential source of systematic difference.

A likely source of systematic uncertainty driving the difference between our AGNLFs and the literature (Akins et al. 2024; Kokorev et al. 2024; Greene et al. 2024) is that the literature AGNLFs are calculated for photometrically selected compact and red sources, many of which are LRDs. We did not apply any such selection to our sample. The largest difference between our results and the literature is observed in the $7.5 \leq z < 9.5$ bin where our results are ≈ 1 dex below the literature. Indeed, this difference is similar to the fraction of sources in that redshift bin that were better fit with ProStellar+AGN compared to ProStellar , $\log_{10}(522/2786) \approx -0.73$, as presented in Figure 7.

In the lowest redshift bin for the AGNLF, there is a significant excess number density for $L_{\text{AGN}} > 10^{46} \text{ erg s}^{-1}$, lining up with the upper range of reported L_{AGN} of LRDs (e.g., Akins et al. 2024; Kokorev et al. 2024). The SEDs of these galaxies showed the characteristic ‘v-shape’ of little red dots (LRDs), with dominant AGN emission toward red wavelengths.

The SMF and SFRF show general agreement with both hydrodynamical (e.g., SIMBA, FLARES, Davé et al. 2019; Lovell et al. 2021; Vijayan et al. 2021) and semi-analytic (e.g., SHARK, Lagos et al. 2024) models⁴ up to $z \approx 9.5$. With the exception of SHARK, at $z > 9.5$ the simulations show a dearth of resolved galaxies, $M_* \lesssim 10^{8.5}$, making it difficult to compare against these observations.

SHARK, however, employs the P-Millennium dark-matter only simulation (Baugh et al. 2019) as the basis for the semi-analytic model to achieve better resolution of low mass galaxies and smaller time increments between snapshots compared to the first version presented

⁴ Every simulation shown is the ‘fiducial’ model as reported in their introductory papers.

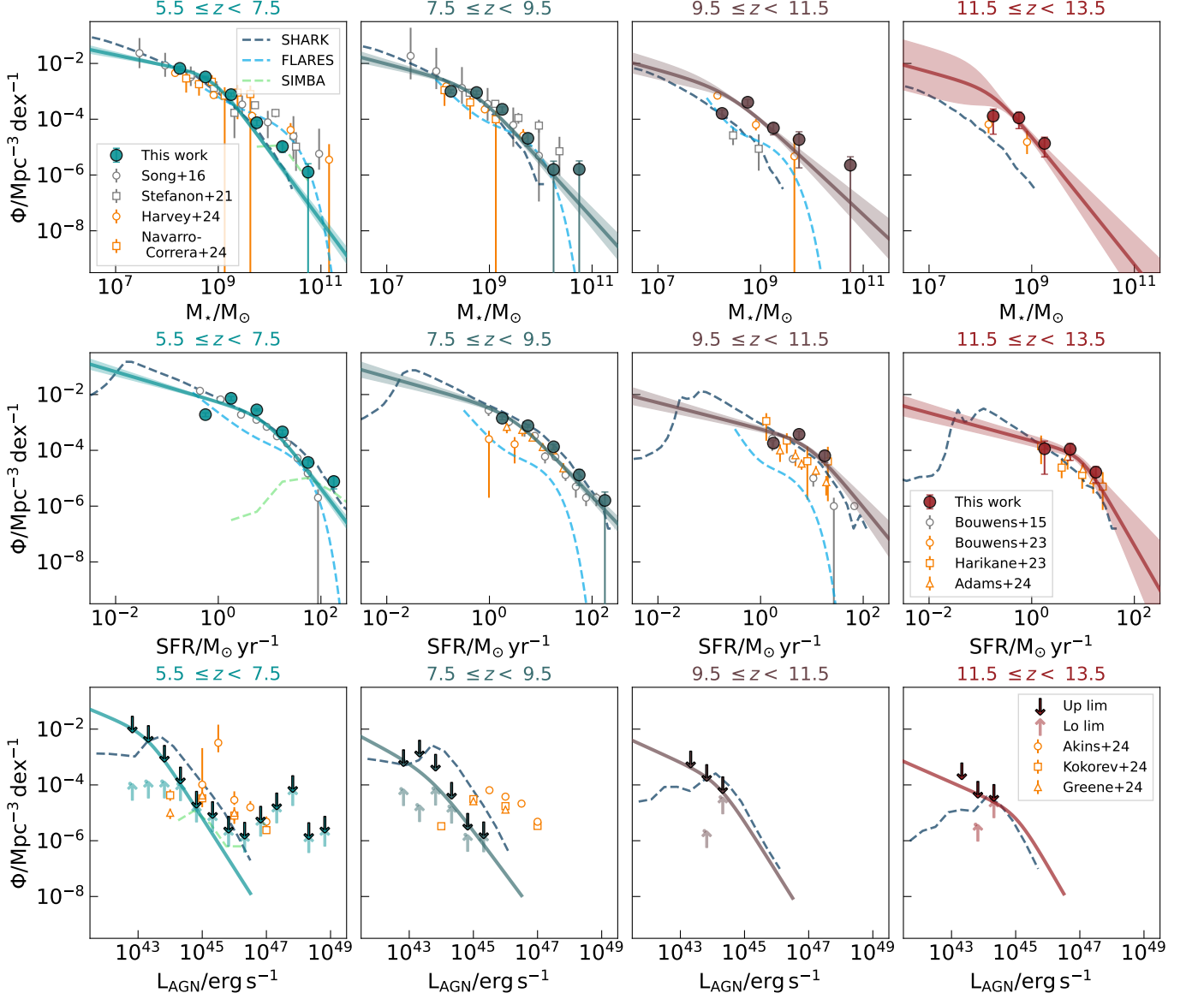


Figure 9. Number density distributions of M_* (*top*), SFR (*middle*) and L_{AGN} (*bottom*), computed at $z = 5.5 - 7.5$ (*leftmost*), $z = 7.5 - 9.5$, $z = 9.5 - 11.5$ and $z = 11.5 - 13.5$ (*rightmost*). In each panel, the double power law function fits and 1σ uncertainty ranges are shown as solid lines and shaded regions, with the color transitioning from blue to red at $z = 5.5 \rightarrow 13.5$. Filled points and 1σ error bars show the binned $1/V_{\text{max}}$ distributions (some of the error bars are smaller than the points). For the AGNLF, the downward facing arrows show the upper limit L_{AGN} and the upward facing arrows show the equivalent lower limit, explained in Section 4.2. We only fitted the L_{AGN} upper limits and restricted the fit to $L_{\text{AGN}} < 10^{46} \text{ erg s}^{-1}$. Comparisons to the literature were obtained from Song et al. (2016); Stefanon et al. (2021); Harvey et al. (2024); Navarro-Carrera et al. (2024) for the SMF, Bouwens et al. (2015, 2023); Harikane et al. (2023); Adams et al. (2024) for the SFRF and Akins et al. (2024); Kokorev et al. (2024); Greene et al. (2024) for the AGNLF. The SFRF literature comparisons are UV luminosity number density measurements converted to SFR as $\text{SFR} = 0.63 \times 1.28 \times 10^{-28} \times L_{\text{UV}}$, where L_{UV} is the UV luminosity at 1500 \AA in units of $\text{erg s}^{-1} \text{ Hz}^{-1}$ and the factor of 0.63 is the relevant conversion of a Salpeter to Chabrier IMF. Results from both hydrodynamical (e.g., SIMBA, FLARES, Davé et al. 2019; Lovell et al. 2021; Vijayan et al. 2021) and semi-analytic (e.g., SHARK, Lagos et al. 2018, 2024) models are shown as dashed lines.

in Lagos et al. (2018). Our results for the SMF and SFRF at all redshifts are generally in agreement with SHARK for the domain of M_* and SFR that we probe. The AGNLF in SHARK is in general ≈ 1 dex higher in normalization with a steeper bright-end slope compared to our results in all redshift bins.

We remark that the simulations themselves show differences that are manifested from their respective implementation of the physical model, despite converging upon the $z \approx 0$ SMF. Recently, Lagos et al. (2025) showed that the different implementation of AGN feedback in these simulations (plus a few others analyzed in that paper) led to galaxies quenching very differently at $z \gtrsim 5$, leading to different formation histories and connections with SMBH properties. While beyond the scope of this work, JWST is well suited to start distinguishing between models in the high redshift frontier (e.g., Shen et al. 2022; D’Silva et al. 2023b).

5.4. Cosmic SMH/SFRH/AGNH

The cosmic evolution of M_* , SFR, L_{AGN} summarizes the history of baryon conversion and astrophysical photon production from the present day to within the first few hundreds of millions of years after the Big Bang. The cosmic evolution is found by taking the distributions in each redshift bin presented in Section 5.3 and integrating them as follows:

$$\rho_X = \int_{X_{lo}}^{X_{hi}} X \times \Phi(X) dX, \quad (12)$$

where $\Phi(X)$ is the number density distribution per unit comoving volume of the astrophysical quantity X .

Numerically, the integration limits should subtend to infinity for a complete census of M_* , SFR, L_{AGN} . Physically, however, these quantities must vanish at some finite lower and upper limit, and so, the integration limits for M_* , SFR, L_{AGN} were chosen to encompass ≈ 5 decades of the quantity in question. As can be seen in Figure 10, the density distributions for M_* , SFR and L_{AGN} , the integrands of Equation 12, are unimodal and concave-downward meaning that the integrals over the entire domain are convergent. Contributions to the integral are ever diminishing for values of the domain far beyond the peak. In the highest redshift bin, we also calculated the direct sum of each quantity per unit comoving volume since the integrals rely on the most significant extrapolations of the fitted distributions. We did this in every redshift bin for the L_{AGN} as our calculation for the CAGNH lower bound, using the $L_{\text{AGN}}^{\text{lo lim}}$ for the ProStellar preferred fits. We omitted $L_{\text{AGN}} < 10^{46}$ erg s $^{-1}$ because of the upturn in the number densities, as shown in Figure 9.

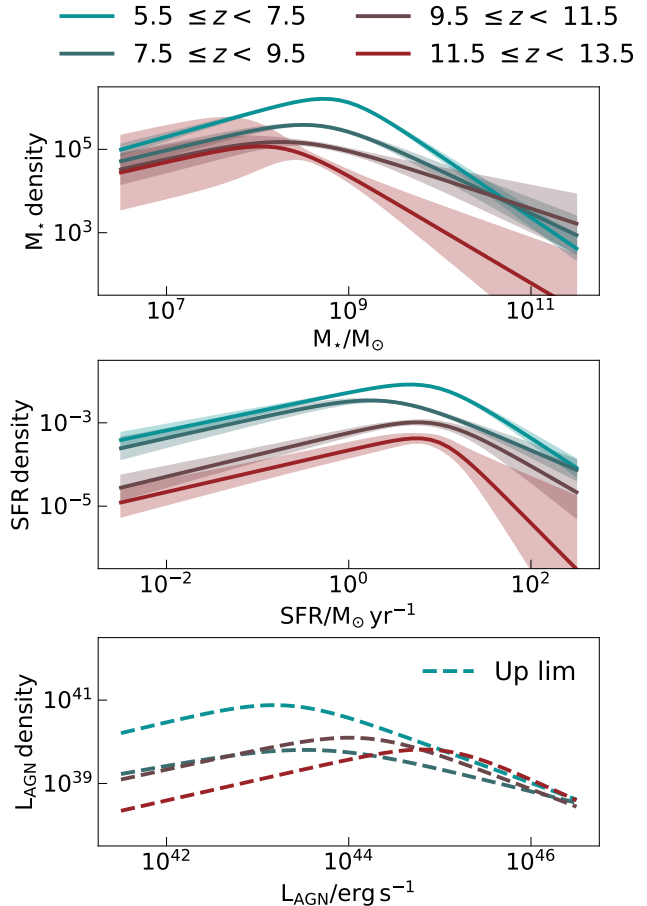


Figure 10. Density distributions of M_* (top), SFR (middle) and L_{AGN} (bottom), obtained from Equation 12 and using the fitted double power law functions from Figure 9. A similar color scheme is used here as in Figure 9.

Figure 11 shows the redshift evolution of ρ_{M_*} , ρ_{SFR} and $\rho_{L_{\text{AGN}}}$, all obtained from integrating the density distributions directly. The lower limit, summed quantities, are shown as upward facing arrows.

For the CSFH and the CAGNH we fitted `massfunc_snorm_trunc` functions (Eqs. 1-5 in D’Silva et al. 2023c)⁵ to the combined results from D’Silva et al. (2023c) at $z \lesssim 3$ and this work. This is the same functional form used to parametrize galaxy SFHs in PROSPECT and is essentially a skewed, unimodal, normal distribution. For the CAGNH we fitted the mid points of the lower and upper limits. The highest redshift point from D’Silva et al. (2023c) was excluded in the CSFH/CAGNH fitting because their data suffered the greatest selection effects in that bin. We obtained a model CSMH by integrating the fitted CSFH and

⁵ We fitted with respect to z , using `magemax = 30` and `mtrunc = 2`

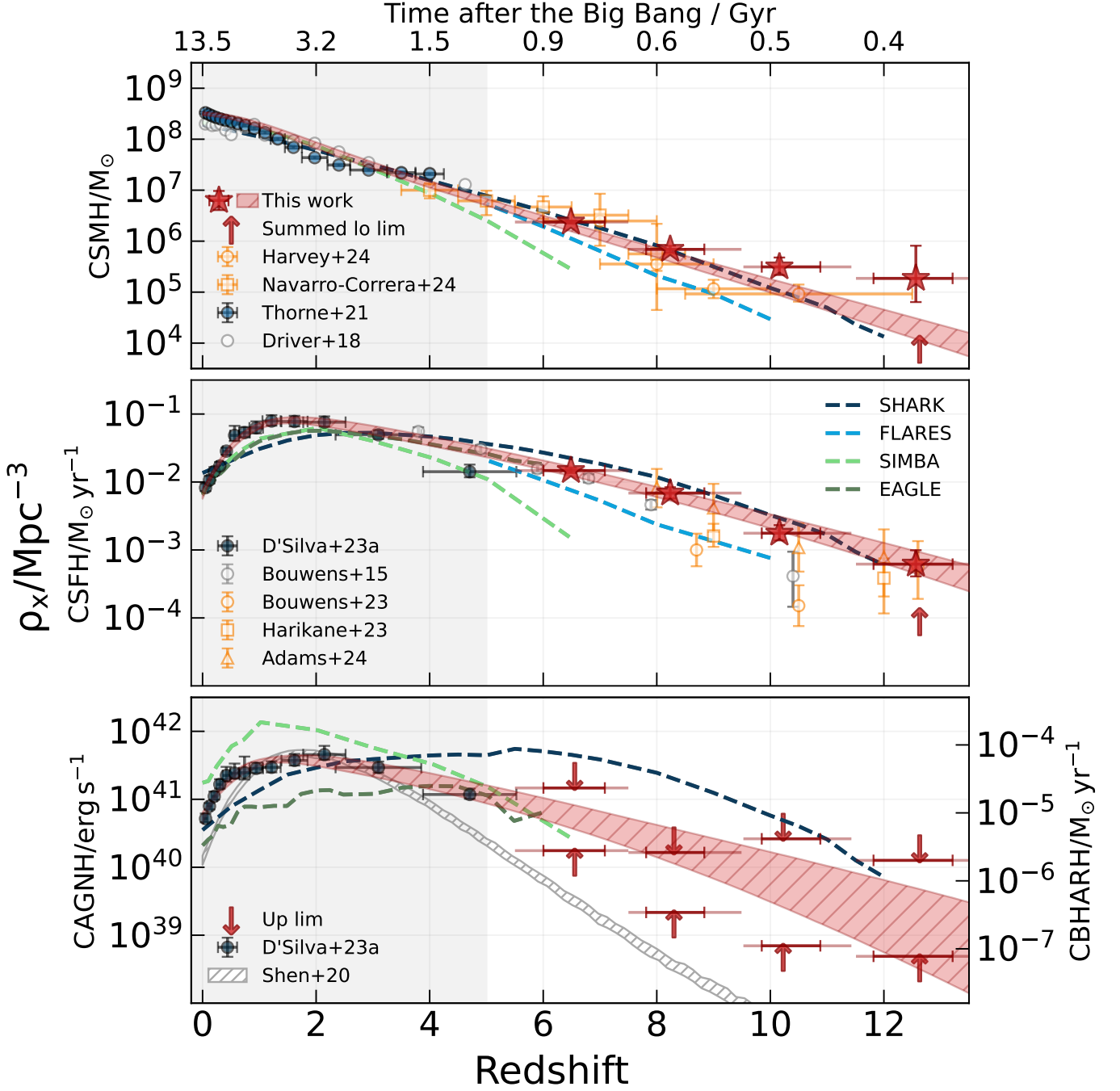


Figure 11. *Top:* Cosmic stellar mass history. The novel results of this work and their 1σ uncertainties are shown as red stars with error bars. The horizontal error bars show both the 1σ of the redshift distribution in the bin and the edges of the redshift bin. The red, filled lines show the corresponding model fits to the data and the 16th-84th percentile ranges. Upward facing arrows show the direct summed quantities in the highest redshift bin. Results from Thorne et al. (2021); Driver et al. (2018); Harvey et al. (2024); Navarro-Carrera et al. (2024) are shown for comparison, as per the figure legend. The grey shaded region marks the state-of-the-art SED fitting results before JWST ($z \lesssim 5$). *Middle:* Cosmic star formation history. The color scheme is the same as the top panel. Results from D’Silva et al. (2023c); Bouwens et al. (2015, 2023); Harikane et al. (2023); Adams et al. (2024) are shown for comparison. *Bottom:* Cosmic AGN luminosity history. The color scheme is the same as the top panel. The upward facing arrows show the results for the direct sum quantities, summing only $L_{\text{AGN}} \leq 10^{46} \text{ erg s}^{-1}$ and the downward facing arrows show the results for the L_{AGN} upper limits. The mid point of this lower and upper bound was used to fit the red, filled lines. Results from D’Silva et al. (2023c); Shen et al. (2020) are shown for comparison. The cosmic black hole accretion rate history is computed as $\rho_{\text{BHAR}} = \rho_{\text{LAGN}} / \epsilon c^2$, where $\epsilon = 0.1$ is the radiative efficiency and c is the speed of light. In all panels, results from both hydrodynamical (e.g., SIMBA, EAGLE, FLARES, Davé et al. 2019; Schaye et al. 2015; Crain et al. 2015; Furlong et al. 2015; Lovell et al. 2021; Vijayan et al. 2021) and semi-analytic (e.g., SHARK, Lagos et al. 2018, 2024) models are shown as dashed lines.

assuming a 41% return fraction for all galaxies and at all redshifts, which is appropriate for a Chabrier IMF (Madau & Dickinson 2014).

That our points for the CSFH are consistent with previous literature results is interesting as D’Silva et al. (2023a) found a tentative ≈ 0.4 dex reduction in the CSFH compared to the same literature values at $z \gtrsim 9.5$ when also including an AGN component in the SED fitting. This inclusion was hence inferred as a pathway to alleviate the tension of excessive star formation compared to models of typical baryon conversion efficiencies inside of dark matter haloes (e.g., Harikane et al. 2022). This analysis, however, improves on D’Silva et al. (2023a) because we have far greater number statistics at $z \gtrsim 9.5$ and also used the BIC to decide between PROStellar and PROStellar+AGN models, suggesting that we cannot entirely explain the difference of the observational CSFH to the typical models as AGN contamination. Despite this, we found that the M_* between PROSPECT runs can vary significantly, in tune with the findings of D’Silva et al. (2023a), meaning that AGN activity is nevertheless a non-negligible aspect to consider when modeling SEDs at these redshifts. Concerning the efficiency of star formation, we note that SHARK shows ≈ 0.5 dex higher CSFH compared to our results at $z \approx 5.5 - 10.5$, due especially to the presence of faint galaxies, demonstrating that the observed abundance of CSFH at these redshifts is somewhat reconcilable with physical models of star formation in dark matter halos.

All three of these quantities exhibit a steady rise over $z = 13.5 \rightarrow 5.5$. The CSMH rises by ≈ 2.6 dex and the CSFH rises by ≈ 1.8 dex, demonstrating the rapid assembly of stellar mass shortly after the Big Bang and up to the peak of CSFH at $z \approx 1 - 2$. The CAGNH on the other hand rises on average by ≈ 2.2 dex over $z = 13.5 \rightarrow 5.5$, suggesting that the growth of SMBHs tends to outpace the assembly of stars in their host galaxies at $z > 5.5$ (e.g., Maiolino et al. 2023; Pacucci et al. 2023; Kormendy & Ho 2013). Both star formation and accretion on the SMBH are fueled by the gas supply, so if star formation is efficient we might further anticipate AGN power to behave similarly. Our fitted CAGNH is $\gtrsim 1$ dex greater at $z \gtrsim 5.5$ throughout compared to the measurements from Shen et al. (2020), who compute AGN bolometric luminosity functions from $z \approx 0 - 7$.

5.5. Quantifying baryon conversion

The phase of the baryon budget usable for fueling star formation and SMBH accretion (e.g., largely molecular instead of atomic or ionized) was in a surplus during these earliest epochs (Lagos et al. 2011), especially at $z \gtrsim 5.5$. As galaxies were only ramping up their star

formation and SMBH accretion, they were yet to deplete the supply of the usable reservoir. Additionally, we can expect that feedback from star formation and SMBH accretion was yet to adequately heat the gas and prevent it from entering the necessary cool phase for fueling, and/or eject it from the galaxy (e.g., Schaye et al. 2010).

To quantify baryon conversion, we computed the cosmic black hole accretion rate history (CBHARH) as

$$\text{CBHARH} = \text{CAGNH} / \epsilon c^2, \quad (13)$$

where $\epsilon = 0.1$ is the radiative efficiency and c is the speed of light, and divide that by the CSFH for a dimensionless baryon conversion ratio. Comparing this ratio of the fitted CSFH and CBHARH, we see that the CBHARH experiences a greater increase from $z \approx 13.5 \rightarrow 5.5$ than the CSFH by a factor of ≈ 2.6 . This increase is insensitive to the choice of constant radiative efficiency, ϵ , that can vary between $0.06 - 0.4$ depending on the spin of the SMBH (e.g., Shakura & Sunyaev 1973). In a follow up paper (D’Silva in prep), we will investigate the affect of the CSFH and CBHARH on reionization.

6. CAVEATS

While we have endeavored to be as consistent and conservative as possible in preparing this work with the data and tools on hand, systematic uncertainties are likely to be underrepresented. We here discuss sources of systematic uncertainties and prospects for the future.

6.1. Photometric redshifts

In the absence of spectroscopic confirmation, we can only compute z_{phot} up to a certain confidence level. This is especially pertinent in the high redshift frontier because the limited photometric bands from even the combination of HST and JWST, means spectral features are sparsely sampled. The results of Sections 4.1 and 4.2 have demonstrated that template incompleteness may be a significant source of uncertainty in template fitting codes. Fortunately, as the NIRSPEC spectroscopic database continues to grow, this issue can be alleviated.

6.2. SED modelling

Although PROSPECT was designed to be highly flexible, we operate in a constrained mode to inhibit parameter degeneracies. A key assumption is a universal Chabrier IMF. The metal-poor terrain of the early Universe seems to afford the formation of massive, $M_* \approx 100M_\odot$, stars due to the lack of metal-line cooling to effectively fragment the primordial gas clouds at scales smaller than the Jean’s length of unpolluted clouds (e.g., Bromm & Larson 2004). Additionally, this may be a pathway to producing massive seed black holes

either as remnants of population III stellar evolution or via direct collapse (e.g., [Latif & Ferrara 2016](#)). [Harvey et al. \(2024\)](#) showed that adopting a top-heavy IMF when SED fitting JWST galaxies can reduce the M_* of $z \approx 12$ galaxies by ≈ 0.5 dex. Although, the goodness-of-fit between top-heavy and more standard IMFs did not significantly change, indicating that photometry alone cannot discern between alternative IMFs. On the other hand, the implementation of the Chabrier IMF in SHARK was shown to reproduce the observed UV-NIR-FIR properties of galaxies from $0 < z < 10$ ([Lagos et al. 2019](#)).

In terms of the AGN component, [Figure 9](#) shows an excess of $\approx L_{\text{AGN}} \gtrsim 10^{46} \text{ erg s}^{-1}$ AGN number density at $z \approx 5.5 - 7.5$. For $z \gtrsim 5.5$ galaxies, we rely on rest-frame UV to optical wavelengths with this data to separate star formation from AGN when interpreting the SEDs, and it is not yet clear if AGN or stellar emission dominates the SED without redder wavelengths (e.g., [Pérez-González et al. 2024](#); [Kocevski et al. 2024](#)). The abundance of $L_{\text{AGN}} \gtrsim 10^{46} \text{ erg s}^{-1}$ AGN, many of which appear as LRDs, may be overestimated, indicating that SED fitting with only HST and NIRC*am* photometry struggles to accurately constrain the AGN power. With the addition of the Mid-Infrared Instrument (MIRI) on *JWST* to probe into the rest-frame IR at these redshifts, the SEDs of some LRDs have indeed been shown to be adequately described by stellar emission, with potentially sub-dominant AGN contributions ([Pérez-González et al. 2024](#); [Williams et al. 2024](#)). Better understanding the effect of the modeling assumptions remains an exciting challenge for the community.

6.3. Obscured AGN growth

Because the data on hand do not probe red enough wavelengths we cannot extract any hidden population of obscured AGN that may exist at $z \gtrsim 5.5$. MIRI observations certainly alleviate this situation by probing further into the thermal emission of the dusty torus. Indeed, MIRI has discovered populations of MIR bright AGN at $z \approx 0 - 5$ ([Yang et al. 2023](#)) without significant X-ray detections. Analyses of LRDs report that the weak X-ray emission cannot be entirely explained by optically thick tori because the required absorber column densities ($N_{\text{H}} \gtrsim 10^{24} - 10^{25} \text{ cm}^{-2}$) are far higher than expected for typical type-1 AGN ($N_{\text{H}} \gtrsim 10^{20} - 10^{23} \text{ cm}^{-2}$, [Ananna et al. 2024](#); [Yue et al. 2024](#); [Kocevski et al. 2024](#)). [Lyu et al. \(2024\)](#) report that $\approx 80\%$ of MIRI identified AGN are lacking X-ray detections that, if not due to optically thick torii, may be a result of intrinsic X-ray faintness due to the absence of strong corona at low metallicity.

Additionally, we have treated all of our galaxies as singular spatial units, employing the same attenuation law via PROSPECT over the entire geography of each galaxy. AGN activity is however confined to the innermost regions of galaxies that, at least in nearby galaxies, exhibits the greatest obscuration ([Kim et al. 2019](#)). As such, we may also be missing a proportion of the AGN activity because of the inability to observe spatially resolved trends in these $z \gtrsim 5.5$ galaxies.

Whether NIRC*am* has missed a significant fraction of obscured AGN activity remains to be confirmed. This situation can improve by turning to spectroscopic observations of broad components in the H α line (e.g., [Larson et al. 2023](#)) and/or metallicity-independent emission line ratio diagnostics (e.g., [Übler et al. 2023](#)), along with further deep, high resolution, multiwavelength constraints from X-rays, MIRI, Sub-mm and beyond. A future work will analyze the X-ray properties of these sources also detected in the NuSTAR NEP survey, thus providing insights into the AGN obscuration.

6.4. Survey variance

According to the survey variance calculator⁶ of [Driver & Robotham \(2010\)](#), survey variance in our fields varies from $\approx 57\%$ in the smallest PEARLS parallel fields in the highest redshift bin to $\approx 20\%$ in the largest PRIMER COSMOS in the lowest redshift bin. The situation improves by combining the fields. Employing the volume-weighted sum of squares method of [Moster et al. \(2011\)](#), suggests $\approx 2\%$ survey variance in the highest redshift bin and $\lesssim 1\%$ in the lowest. Survey variance may however increase toward lower M_* , SFR and L_{AGN} where the constraining power comes from deep, narrow surveys like JADES and NGDEEP; but, as can be seen from [Figure 10](#), contributions to the density from lower values diminish. Hence, we expect that survey variance is a sub-dominant source of uncertainty compared to the others discussed in this section. As the JWST database continues to expand cosmic variance will be further reduced.

7. SUMMARY

JWST continues to enlighten our grasp of star formation and AGN from $z \approx 13.5 \rightarrow 5.5$. For the first time, the interface of star formation and the growth of SMBHs has been consistently connected from $z = 0$ to $z = 13.5$, encompassing $\gtrsim 13$ Gyr of cosmic time. The key results are:

⁶ <https://cosmocalc.icrar.org/>

- The novel, open-source software suite JUMPROPE for processing JWST images was described. JUMPROPE is an all-in-one package that can query the MAST archive, calibrate images using the JWST Calibration Pipeline, remove $1/f$ noise and wisp artifacts, produce mosaics with PROPANE and finally perform multi-band measurements with PROFOUND.
- We searched for $z \gtrsim 5.5$ galaxies from 400 arcmin^2 of JWST fields processed with JUMPROPE (see Table 1). A sample of 3947 $z \approx 5.5 - 13.5$ galaxies was obtained with a two-phased photometric redshift approach, striving for 95% completeness. Redshifts for the high redshift sample were initially obtained using EAZY and then refined by further SED fitting with PROSPECT. With the PROSPECT SED fits we obtained the M_* , SFR and L_{AGN} .
- We performed two sets of PROSPECT SED fits: (i). $\text{Pro}_{\text{Stellar}}$ where only stellar components were used to characterise the SEDs (ii). $\text{Pro}_{\text{Stellar}+\text{AGN}}$ that also included an AGN component. The BIC was used to determine which model was preferred. For the galaxies with preferred $\text{Pro}_{\text{Stellar}}$ fits, we considered two extremes of AGN contribution to the SED: $L_{\text{AGN}}^{\text{lo lim}} = 0$ and $L_{\text{AGN}}^{\text{up lim}}$ that was found from an unobscured AGN template that contributed no more than 20% of the flux in the combined F277W+F356W+F444W filters. This allowed us to compute a lower and upper bound of possible AGN contribution to these galaxy SEDs.
- The inferred M_* , SFR and L_{AGN} were used to compute the SMF, SFRF and AGNLF in four redshift bins at $z \approx 5.5 - 13.5$. We computed both binned quantities and double power-law fits (Equation 11) with DFTOOLS. However, to fit the AGNLF we could only use the $L_{\text{AGN}}^{\text{up lim}}$ for the $\text{Pro}_{\text{Stellar}}$ preferred SED fits.
- The SMF, SFRF and AGNLF were integrated to then compute the CSMH, CSFH and CAGNH. Our results for the CSMH, CSFH and CAGNH are consistent with previous results in the literature. The CAGNH rises by ≈ 2.2 dex compared to ≈ 1.8 dex for the CSFH over the same redshift

range, indicating that SMBH growth tends to outpace the assembly of stellar mass.

- Systematic uncertainties remain an obstruction to further deciphering the mysteries of the early Universe. Fortunately, this situation can only get better as JWST continues to build up its imaging and spectroscopic database, to be used in harmony with multiwavelength facilities covering the breadth of the electromagnetic spectrum.

DATA AVAILABILITY

All the data for the fields used in this work are available [here](#). The processing pipeline JUMPROPE can be found on [GitHub](#). Catalogues will be made available upon reasonable request to the corresponding author.

ACKNOWLEDGEMENTS

J.C.J.D is supported by the Australian Government Research Training Program (RTP) Scholarship. CL is a recipient of the ARC Discovery Project DP210101945. ASGR acknowledges funding by the Australian Research Council (ARC) Future Fellowship scheme (FT200100375). NA, TH and C.J.C acknowledge support from the ERC Advanced Investigator Grant EPOCHS (788113). RAW, SHC, and RAJ acknowledge support from NASA JWST Interdisciplinary Scientist grants NAG5-12460, NNX14AN10G and 80NSSC18K0200 from GSFC. CNAW acknowledges funding from the JWST/NIRCam contract NASS-0215 to the University of Arizona.

This research was supported by the Australian Research Council Centre of Excellence for All Sky Astrophysics in 3 Dimensions (ASTRO 3D), through project number CE170100013. This work was supported by resources provided by The Pawsey Supercomputing Centre with funding from the Australian Government and the Government of Western Australia.

This work is based on observations made with the NASA/ESA Hubble Space Telescope (*HST*) and NASA/ESA/CSA James Webb Space Telescope (*JWST*) obtained from the Mikulski Archive for Space Telescopes (MAST) at the Space Telescope Science Institute (STScI), which is operated by the Association of Universities for Research in Astronomy, Inc., under NASA contract NAS 5-03127 for *JWST*, and NAS 5-26555 for *HST*. The observations used in this work are associated with *JWST* programs 1176, 2738, 1345, 2079, 1180, 1210, 3250 and 1837. We acknowledge all those involved in the development of the *JWST* and the execution of these large observing programs.

REFERENCES

- Acquaviva, V., Raichoor, A., & Gawiser, E. 2015, *ApJ*, 804, 8, doi: [10.1088/0004-637X/804/1/8](https://doi.org/10.1088/0004-637X/804/1/8)
- Adams, N. J., Conselice, C. J., Austin, D., et al. 2024, *ApJ*, 965, 169, doi: [10.3847/1538-4357/ad2a7b](https://doi.org/10.3847/1538-4357/ad2a7b)
- Akins, H. B., Casey, C. M., Lambrides, E., et al. 2024, COSMOS-Web: The over-Abundance and Physical Nature of "Little Red Dots"—Implications for Early Galaxy and SMBH Assembly, arXiv. <https://arxiv.org/abs/2406.10341>
- Ananna, T. T., Bogdán, Á., Kovács, O. E., Natarajan, P., & Hickox, R. C. 2024, *ApJL*, 969, L18, doi: [10.3847/2041-8213/ad5669](https://doi.org/10.3847/2041-8213/ad5669)
- Arrabal Haro, P., Dickinson, M., Finkelstein, S. L., et al. 2023, *ApJ*, 951, L22, doi: [10.3847/2041-8213/acdd54](https://doi.org/10.3847/2041-8213/acdd54)
- Arrabal Haro, P., Dickinson, M., Finkelstein, S. L., et al. 2023, *Nature*, 622, 707, doi: [10.1038/s41586-023-06521-7](https://doi.org/10.1038/s41586-023-06521-7)
- Atek, H., Richard, J., Kneib, J.-P., & Schaerer, D. 2018, *MNRAS*, 479, 5184, doi: [10.1093/mnras/sty1820](https://doi.org/10.1093/mnras/sty1820)
- Bagley, M. B., Finkelstein, S. L., Koekemoer, A. M., et al. 2023, *ApJL*, 946, L12, doi: [10.3847/2041-8213/acbb08](https://doi.org/10.3847/2041-8213/acbb08)
- Bagley, M. B., Pirzkal, N., Finkelstein, S. L., et al. 2024, *ApJL*, 965, L6, doi: [10.3847/2041-8213/ad2f31](https://doi.org/10.3847/2041-8213/ad2f31)
- Baldwin, J. A., Phillips, M. M., & Terlevich, R. 1981, *PASP*, 93, 5, doi: [10.1086/130766](https://doi.org/10.1086/130766)
- Baugh, C. M., Gonzalez-Perez, V., Lagos, C. D. P., et al. 2019, *MNRAS*, 483, 4922, doi: [10.1093/mnras/sty3427](https://doi.org/10.1093/mnras/sty3427)
- Behroozi, P. S., Wechsler, R. H., & Conroy, C. 2013, *ApJ*, 770, 57, doi: [10.1088/0004-637X/770/1/57](https://doi.org/10.1088/0004-637X/770/1/57)
- Bellstedt, S., Driver, S. P., Robotham, A. S. G., et al. 2020a, *MNRAS*, 496, 3235, doi: [10.1093/mnras/staa1466](https://doi.org/10.1093/mnras/staa1466)
- Bellstedt, S., Robotham, A. S. G., Driver, S. P., et al. 2020b, *MNRAS*, 498, 5581, doi: [10.1093/mnras/staa2620](https://doi.org/10.1093/mnras/staa2620)
- Bouwens, R. J., Illingworth, G. D., Ellis, R. S., Oesch, P. A., & Stefanon, M. 2022, *ApJ*, 940, 55, doi: [10.3847/1538-4357/ac86d1](https://doi.org/10.3847/1538-4357/ac86d1)
- Bouwens, R. J., Illingworth, G. D., Oesch, P. A., et al. 2015, *ApJ*, 803, 34, doi: [10.1088/0004-637X/803/1/34](https://doi.org/10.1088/0004-637X/803/1/34)
- Bouwens, R. J., Oesch, P. A., Stefanon, M., et al. 2021, *AJ*, 162, 47, doi: [10.3847/1538-3881/abf83e](https://doi.org/10.3847/1538-3881/abf83e)
- Bouwens, R. J., Stefanon, M., Brammer, G., et al. 2023, *MNRAS*, 523, 1036, doi: [10.1093/mnras/stad1145](https://doi.org/10.1093/mnras/stad1145)
- Brammer, G. B., van Dokkum, P. G., & Coppi, P. 2008, *ApJ*, 686, 1503, doi: [10.1086/591786](https://doi.org/10.1086/591786)
- Brandt, W. N., & Alexander, D. M. 2015, *A&A Rv*, 23, 1, doi: [10.1007/s00159-014-0081-z](https://doi.org/10.1007/s00159-014-0081-z)
- Bromm, V., & Larson, R. B. 2004, *ARA&A*, 42, 79, doi: [10.1146/annurev.astro.42.053102.134034](https://doi.org/10.1146/annurev.astro.42.053102.134034)
- Bruzual, G., & Charlot, S. 2003, *MNRAS*, 344, 1000, doi: [10.1046/j.1365-8711.2003.06897.x](https://doi.org/10.1046/j.1365-8711.2003.06897.x)
- Bunker, A. J., Cameron, A. J., Curtis-Lake, E., et al. 2024, *A&A*, 690, A288, doi: [10.1051/0004-6361/202347094](https://doi.org/10.1051/0004-6361/202347094)
- Chabrier, G. 2003, *PASP*, 115, 763, doi: [10.1086/376392](https://doi.org/10.1086/376392)
- Charlot, S., & Fall, S. M. 2000, *ApJ*, 539, 718, doi: [10.1086/309250](https://doi.org/10.1086/309250)
- Conroy, C. 2013, *ARA&A*, 51, 393, doi: [10.1146/annurev-astro-082812-141017](https://doi.org/10.1146/annurev-astro-082812-141017)
- Conroy, C., & Gunn, J. E. 2010, *ApJ*, 712, 833, doi: [10.1088/0004-637X/712/2/833](https://doi.org/10.1088/0004-637X/712/2/833)
- Conselice, C. J., Adams, N., Harvey, T., et al. 2024, arXiv e-prints, arXiv:2407.14973, doi: [10.48550/arXiv.2407.14973](https://doi.org/10.48550/arXiv.2407.14973)
- Crain, R. A., Schaye, J., Bower, R. G., et al. 2015, *MNRAS*, 450, 1937, doi: [10.1093/mnras/stv725](https://doi.org/10.1093/mnras/stv725)
- Dale, D. A., Helou, G., Magdis, G. E., et al. 2014, *ApJ*, 784, 83, doi: [10.1088/0004-637X/784/1/83](https://doi.org/10.1088/0004-637X/784/1/83)
- Davé, R., Anglés-Alcázar, D., Narayanan, D., et al. 2019, *MNRAS*, 486, 2827, doi: [10.1093/mnras/stz937](https://doi.org/10.1093/mnras/stz937)
- Davies, L. J. M., Robotham, A. S. G., Driver, S. P., et al. 2018, *MNRAS*, 480, 768, doi: [10.1093/mnras/sty1553](https://doi.org/10.1093/mnras/sty1553)
- Davies, L. J. M., Thorne, J. E., Robotham, A. S. G., et al. 2021, *MNRAS*, 506, 256, doi: [10.1093/mnras/stab1601](https://doi.org/10.1093/mnras/stab1601)
- Davies, L. J. M., Thorne, J. E., Bellstedt, S., et al. 2022, *MNRAS*, 509, 4392, doi: [10.1093/mnras/stab3145](https://doi.org/10.1093/mnras/stab3145)
- Donnan, C. T., McLure, R. J., Dunlop, J. S., et al. 2024, *MNRAS*, 533, 3222, doi: [10.1093/mnras/stae2037](https://doi.org/10.1093/mnras/stae2037)
- Driver, S. P., & Robotham, A. S. G. 2010, *MNRAS*, 407, 2131, doi: [10.1111/j.1365-2966.2010.17028.x](https://doi.org/10.1111/j.1365-2966.2010.17028.x)
- Driver, S. P., Hill, D. T., Kelvin, L. S., et al. 2011, *MNRAS*, 413, 971, doi: [10.1111/j.1365-2966.2010.18188.x](https://doi.org/10.1111/j.1365-2966.2010.18188.x)
- Driver, S. P., Andrews, S. K., da Cunha, E., et al. 2018, *MNRAS*, 475, 2891, doi: [10.1093/mnras/stx2728](https://doi.org/10.1093/mnras/stx2728)
- Driver, S. P., Bellstedt, S., Robotham, A. S. G., et al. 2022, *MNRAS*, 513, 439, doi: [10.1093/mnras/stac472](https://doi.org/10.1093/mnras/stac472)
- D’Silva, J. C. J., Driver, S. P., Lagos, C. D. P., et al. 2023a, *ApJL*, 959, L18, doi: [10.3847/2041-8213/ad103e](https://doi.org/10.3847/2041-8213/ad103e)
- D’Silva, J. C. J., Lagos, C. D. P., Davies, L. J. M., Lovell, C. C., & Vijayan, A. P. 2023b, *MNRAS*, 518, 456, doi: [10.1093/mnras/stac2878](https://doi.org/10.1093/mnras/stac2878)
- D’Silva, J. C. J., Driver, S. P., Lagos, C. D. P., et al. 2023c, *MNRAS*, 524, 1448, doi: [10.1093/mnras/stad1974](https://doi.org/10.1093/mnras/stad1974)
- Eisenstein, D. J., Willott, C., Alberts, S., et al. 2023, arXiv e-prints, arXiv:2306.02465, doi: [10.48550/arXiv.2306.02465](https://doi.org/10.48550/arXiv.2306.02465)
- Ferreira, L., Conselice, C. J., Sazonova, E., et al. 2023, *ApJ*, 955, 94, doi: [10.3847/1538-4357/acec76](https://doi.org/10.3847/1538-4357/acec76)
- Finkelstein, S. L., Ryan Jr., R. E., Papovich, C., et al. 2015, *ApJ*, 810, 71, doi: [10.1088/0004-637X/810/1/71](https://doi.org/10.1088/0004-637X/810/1/71)

- Finkelstein, S. L., Bagley, M. B., Haro, P. A., et al. 2022, *ApJL*, 940, L55, doi: [10.3847/2041-8213/ac966e](https://doi.org/10.3847/2041-8213/ac966e)
- Finkelstein, S. L., Bagley, M. B., Ferguson, H. C., et al. 2023, *ApJL*, 946, L13, doi: [10.3847/2041-8213/acade4](https://doi.org/10.3847/2041-8213/acade4)
- Fitzpatrick, E. L., & Massa, D. 2007, *ApJ*, 663, 320, doi: [10.1086/518158](https://doi.org/10.1086/518158)
- Fritz, J., Franceschini, A., & Hatziminaoglou, E. 2006, *MNRAS*, 366, 767, doi: [10.1111/j.1365-2966.2006.09866.x](https://doi.org/10.1111/j.1365-2966.2006.09866.x)
- Frye, B. L., Pascale, M., Foo, N., et al. 2023, *ApJ*, 952, 81, doi: [10.3847/1538-4357/acd929](https://doi.org/10.3847/1538-4357/acd929)
- Furlong, M., Bower, R. G., Theuns, T., et al. 2015, *MNRAS*, 450, 4486, doi: [10.1093/mnras/stv852](https://doi.org/10.1093/mnras/stv852)
- Gardner, J. P., Mather, J. C., Clampin, M., et al. 2006, *SSRv*, 123, 485, doi: [10.1007/s11214-006-8315-7](https://doi.org/10.1007/s11214-006-8315-7)
- Gebhardt, K., Bender, R., Bower, G., et al. 2000, *ApJ*, 539, L13, doi: [10.1086/312840](https://doi.org/10.1086/312840)
- Glazebrook, K., Nanayakkara, T., Schreiber, C., et al. 2024, *Nature*, 628, 277, doi: [10.1038/s41586-024-07191-9](https://doi.org/10.1038/s41586-024-07191-9)
- Greene, J. E., Labbe, I., Goulding, A. D., et al. 2024, *ApJ*, 964, 39, doi: [10.3847/1538-4357/ad1e5f](https://doi.org/10.3847/1538-4357/ad1e5f)
- Grogin, N. A., Kocevski, D. D., Faber, S. M., et al. 2011, *ApJS*, 197, 35, doi: [10.1088/0067-0049/197/2/35](https://doi.org/10.1088/0067-0049/197/2/35)
- Harikane, Y., Nakajima, K., Ouchi, M., et al. 2024, *ApJ*, 960, 56, doi: [10.3847/1538-4357/ad0b7e](https://doi.org/10.3847/1538-4357/ad0b7e)
- Harikane, Y., Ono, Y., Ouchi, M., et al. 2022, *ApJS*, 259, 20, doi: [10.3847/1538-4365/ac3dfc](https://doi.org/10.3847/1538-4365/ac3dfc)
- Harikane, Y., Zhang, Y., Nakajima, K., et al. 2023, *ApJ*, 959, 39, doi: [10.3847/1538-4357/ad029e](https://doi.org/10.3847/1538-4357/ad029e)
- Harikane, Y., Ouchi, M., Oguri, M., et al. 2023, *ApJS*, 265, 5, doi: [10.3847/1538-4365/acaaa9](https://doi.org/10.3847/1538-4365/acaaa9)
- Harvey, T., Conselice, C. J., Adams, N. J., et al. 2024, *The Astrophysical Journal*, 978, 89, doi: [10.3847/1538-4357/ad8c29](https://doi.org/10.3847/1538-4357/ad8c29)
- Juodžbalis, I., Conselice, C. J., Singh, M., et al. 2023, *MNRAS*, 525, 1353, doi: [10.1093/mnras/stad2396](https://doi.org/10.1093/mnras/stad2396)
- Kartaltepe, J. S., Rose, C., Vanderhoof, B. N., et al. 2023, *ApJL*, 946, L15, doi: [10.3847/2041-8213/acad01](https://doi.org/10.3847/2041-8213/acad01)
- Katsianis, A., Zheng, X., Gonzalez, V., et al. 2019, *ApJ*, 879, 11, doi: [10.3847/1538-4357/ab1f8d](https://doi.org/10.3847/1538-4357/ab1f8d)
- Kauffmann, G., & Haehnelt, M. 2000, *MNRAS*, 311, 576, doi: [10.1046/j.1365-8711.2000.03077.x](https://doi.org/10.1046/j.1365-8711.2000.03077.x)
- Keel, W. C., Windhorst, R. A., Jansen, R. A., et al. 2023, *AJ*, 165, 166, doi: [10.3847/1538-3881/acbdff](https://doi.org/10.3847/1538-3881/acbdff)
- Kim, D., Jansen, R. A., Windhorst, R. A., Cohen, S. H., & McCabe, T. J. 2019, *ApJ*, 884, 21, doi: [10.3847/1538-4357/ab385c](https://doi.org/10.3847/1538-4357/ab385c)
- Kocevski, D. D., Onoue, M., Inayoshi, K., et al. 2023, *ApJ*, 954, L4, doi: [10.3847/2041-8213/ace5a0](https://doi.org/10.3847/2041-8213/ace5a0)
- Kocevski, D. D., Finkelstein, S. L., Barro, G., et al. 2024, *The Rise of Faint, Red AGN at $z > 4$: A Sample of Little Red Dots in the JWST Extragalactic Legacy Fields*, doi: [10.48550/arXiv.2404.03576](https://doi.org/10.48550/arXiv.2404.03576)
- Koekemoer, A. M., Faber, S. M., Ferguson, H. C., et al. 2011, *ApJS*, 197, 36, doi: [10.1088/0067-0049/197/2/36](https://doi.org/10.1088/0067-0049/197/2/36)
- Kokorev, V., Caputi, K. I., Greene, J. E., et al. 2024, *ApJ*, 968, 38, doi: [10.3847/1538-4357/ad4265](https://doi.org/10.3847/1538-4357/ad4265)
- Kormendy, J., & Ho, L. C. 2013, *ARA&A*, 51, 511, doi: [10.1146/annurev-astro-082708-101811](https://doi.org/10.1146/annurev-astro-082708-101811)
- Labbé, I., van Dokkum, P., Nelson, E., et al. 2023, *Nature*, 616, 266, doi: [10.1038/s41586-023-05786-2](https://doi.org/10.1038/s41586-023-05786-2)
- Lagos, C. D. P., Baugh, C. M., Lacey, C. G., et al. 2011, *MNRAS*, 418, 1649, doi: [10.1111/j.1365-2966.2011.19583.x](https://doi.org/10.1111/j.1365-2966.2011.19583.x)
- Lagos, C. d. P., Tobar, R. J., Robotham, A. S. G., et al. 2018, *MNRAS*, 481, 3573, doi: [10.1093/mnras/sty2440](https://doi.org/10.1093/mnras/sty2440)
- Lagos, C. d. P., Robotham, A. S. G., Trayford, J. W., et al. 2019, *MNRAS*, 489, 4196, doi: [10.1093/mnras/stz2427](https://doi.org/10.1093/mnras/stz2427)
- Lagos, C. d. P., Bravo, M., Tobar, R., et al. 2024, *MNRAS*, 531, 3551, doi: [10.1093/mnras/stae1024](https://doi.org/10.1093/mnras/stae1024)
- Lagos, C. d. P., Valentino, F., Wright, R. J., et al. 2025, *Monthly Notices of the Royal Astronomical Society*, 536, 2324, doi: [10.1093/mnras/stae2626](https://doi.org/10.1093/mnras/stae2626)
- Langeroodi, D., & Hjorth, J. 2023, *ApJL*, 957, L27, doi: [10.3847/2041-8213/acfeec](https://doi.org/10.3847/2041-8213/acfeec)
- Larson, R. L., Finkelstein, S. L., Kocevski, D. D., et al. 2023, *ApJL*, 953, L29, doi: [10.3847/2041-8213/ace619](https://doi.org/10.3847/2041-8213/ace619)
- Larson, R. L., Hutchison, T. A., Bagley, M., et al. 2023, *ApJ*, 958, 141, doi: [10.3847/1538-4357/acfed4](https://doi.org/10.3847/1538-4357/acfed4)
- Latif, M. A., & Ferrara, A. 2016, *PASA*, 33, e051, doi: [10.1017/pasa.2016.41](https://doi.org/10.1017/pasa.2016.41)
- Leethochawalit, N., Trenti, M., Morishita, T., Roberts-Borsani, G., & Treu, T. 2022, *MNRAS*, 509, 5836, doi: [10.1093/mnras/stab3265](https://doi.org/10.1093/mnras/stab3265)
- Lotz, J. M., Koekemoer, A., Coe, D., et al. 2017, *ApJ*, 837, 97, doi: [10.3847/1538-4357/837/1/97](https://doi.org/10.3847/1538-4357/837/1/97)
- Lovell, C. C., Harrison, I., Harikane, Y., Tacchella, S., & Wilkins, S. M. 2023, *MNRAS*, 518, 2511, doi: [10.1093/mnras/stac3224](https://doi.org/10.1093/mnras/stac3224)
- Lovell, C. C., Vijayan, A. P., Thomas, P. A., et al. 2021, *MNRAS*, 500, 2127, doi: [10.1093/mnras/staa3360](https://doi.org/10.1093/mnras/staa3360)
- Lyu, J., Alberts, S., Rieke, G. H., et al. 2024, *ApJ*, 966, 229, doi: [10.3847/1538-4357/ad3643](https://doi.org/10.3847/1538-4357/ad3643)
- Madau, P., & Dickinson, M. 2014, *ARA&A*, 52, 415, doi: [10.1146/annurev-astro-081811-125615](https://doi.org/10.1146/annurev-astro-081811-125615)
- Magorrian, J., Tremaine, S., Richstone, D., et al. 1998, *AJ*, 115, 2285, doi: [10.1086/300353](https://doi.org/10.1086/300353)

- Maiolino, R., Scholtz, J., Curtis-Lake, E., et al. 2023, JADES. The Diverse Population of Infant Black Holes at 4, doi: [10.48550/arXiv.2308.01230](https://doi.org/10.48550/arXiv.2308.01230)
- Marley, M. S., Saumon, D., Visscher, C., et al. 2021, ApJ, 920, 85, doi: [10.3847/1538-4357/ac141d](https://doi.org/10.3847/1538-4357/ac141d)
- Matsuoka, Y., Strauss, M. A., Kashikawa, N., et al. 2018, ApJ, 869, 150, doi: [10.3847/1538-4357/aace7a](https://doi.org/10.3847/1538-4357/aace7a)
- Matthee, J., Naidu, R. P., Brammer, G., et al. 2024, ApJ, 963, 129, doi: [10.3847/1538-4357/ad2345](https://doi.org/10.3847/1538-4357/ad2345)
- Merloni, A., & Heinz, S. 2008, MNRAS, 388, 1011, doi: [10.1111/j.1365-2966.2008.13472.x](https://doi.org/10.1111/j.1365-2966.2008.13472.x)
- Moster, B. P., Somerville, R. S., Newman, J. A., & Rix, H.-W. 2011, ApJ, 731, 113, doi: [10.1088/0004-637X/731/2/113](https://doi.org/10.1088/0004-637X/731/2/113)
- Nakajima, K., Ouchi, M., Isobe, Y., et al. 2023, ApJS, 269, 33, doi: [10.3847/1538-4365/acd556](https://doi.org/10.3847/1538-4365/acd556)
- Navarro-Carrera, R., Rinaldi, P., Caputi, K. I., et al. 2024, ApJ, 961, 207, doi: [10.3847/1538-4357/ad0df6](https://doi.org/10.3847/1538-4357/ad0df6)
- Obreschkow, D., Murray, S. G., Robotham, A. S. G., & Westmeier, T. 2018, MNRAS, 474, 5500, doi: [10.1093/mnras/stx3155](https://doi.org/10.1093/mnras/stx3155)
- O'Brien, R., Jansen, R. A., Grogin, N. A., et al. 2024, ApJS, 272, 19, doi: [10.3847/1538-4365/ad3948](https://doi.org/10.3847/1538-4365/ad3948)
- Oesch, P. A., Bouwens, R. J., Illingworth, G. D., Labbé, I., & Stefanon, M. 2018, ApJ, 855, 105, doi: [10.3847/1538-4357/aab03f](https://doi.org/10.3847/1538-4357/aab03f)
- Oke, J. B., & Gunn, J. E. 1983, ApJ, 266, 713, doi: [10.1086/160817](https://doi.org/10.1086/160817)
- Pacucci, F., Nguyen, B., Carniani, S., Maiolino, R., & Fan, X. 2023, ApJL, 957, L3, doi: [10.3847/2041-8213/ad0158](https://doi.org/10.3847/2041-8213/ad0158)
- Padovani, P., Alexander, D. M., Assef, R. J., et al. 2017, A&A Rv, 25, 2, doi: [10.1007/s00159-017-0102-9](https://doi.org/10.1007/s00159-017-0102-9)
- Pérez-González, P. G., Barro, G., Rieke, G. H., et al. 2024, ApJ, 968, 4, doi: [10.3847/1538-4357/ad38bb](https://doi.org/10.3847/1538-4357/ad38bb)
- Planck Collaboration, Ade, P. a. R., Aghanim, N., et al. 2013, A&A, 554, A139, doi: [10.1051/0004-6361/201220271](https://doi.org/10.1051/0004-6361/201220271)
- Rieke, M. J., Robertson, B., Tacchella, S., et al. 2023, ApJS, 269, 16, doi: [10.3847/1538-4365/acf44d](https://doi.org/10.3847/1538-4365/acf44d)
- Robotham, A. S. G., Bellstedt, S., Lagos, C. d. P., et al. 2020, MNRAS, 495, 905, doi: [10.1093/mnras/staa1116](https://doi.org/10.1093/mnras/staa1116)
- Robotham, A. S. G., Davies, L. J. M., Driver, S. P., et al. 2018, MNRAS, 476, 3137, doi: [10.1093/mnras/sty440](https://doi.org/10.1093/mnras/sty440)
- Robotham, A. S. G., D'Silva, J. C. J., Windhorst, R. A., et al. 2023, PASP, 135, 085003, doi: [10.1088/1538-3873/acea42](https://doi.org/10.1088/1538-3873/acea42)
- Robotham, A. S. G., Taranu, D. S., Tobar, R., Moffett, A., & Driver, S. P. 2017, MNRAS, 466, 1513, doi: [10.1093/mnras/stw3039](https://doi.org/10.1093/mnras/stw3039)
- Robotham, A. S. G., Tobar, R., Bellstedt, S., et al. 2024, MNRAS, 528, 5046, doi: [10.1093/mnras/stae349](https://doi.org/10.1093/mnras/stae349)
- Schaye, J., Dalla Vecchia, C., Booth, C. M., et al. 2010, MNRAS, 402, 1536, doi: [10.1111/j.1365-2966.2009.16029.x](https://doi.org/10.1111/j.1365-2966.2009.16029.x)
- Schaye, J., Crain, R. A., Bower, R. G., et al. 2015, MNRAS, 446, 521, doi: [10.1093/mnras/stu2058](https://doi.org/10.1093/mnras/stu2058)
- Schechter, P. 1976, ApJ, 203, 297, doi: [10.1086/154079](https://doi.org/10.1086/154079)
- Schneider, R., Valiante, R., Trinca, A., et al. 2023, MNRAS, 526, 3250, doi: [10.1093/mnras/stad2503](https://doi.org/10.1093/mnras/stad2503)
- Shakura, N. I., & Sunyaev, R. A. 1973, A&A, 24, 337
- Shen, X., Hopkins, P. F., Faucher-Giguère, C.-A., et al. 2020, MNRAS, 495, 3252, doi: [10.1093/mnras/staa1381](https://doi.org/10.1093/mnras/staa1381)
- Shen, X., Vogelsberger, M., Nelson, D., et al. 2022, MNRAS, 510, 5560, doi: [10.1093/mnras/stab3794](https://doi.org/10.1093/mnras/stab3794)
- Song, M., Finkelstein, S. L., Ashby, M. L. N., et al. 2016, ApJ, 825, 5, doi: [10.3847/0004-637X/825/1/5](https://doi.org/10.3847/0004-637X/825/1/5)
- Stefanon, M., Bouwens, R. J., Labbé, I., et al. 2021, ApJ, 922, 29, doi: [10.3847/1538-4357/ac1bb6](https://doi.org/10.3847/1538-4357/ac1bb6)
- Thorne, J. E., Robotham, A. S. G., Davies, L. J. M., et al. 2021, MNRAS, 505, 540, doi: [10.1093/mnras/stab1294](https://doi.org/10.1093/mnras/stab1294)
- Thorne, J. E., Robotham, A. S. G., Bellstedt, S., et al. 2022a, MNRAS, 517, 6035, doi: [10.1093/mnras/stac3082](https://doi.org/10.1093/mnras/stac3082)
- Thorne, J. E., Robotham, A. S. G., Davies, L. J. M., et al. 2022b, MNRAS, 509, 4940, doi: [10.1093/mnras/stab3208](https://doi.org/10.1093/mnras/stab3208)
- Übler, H., Maiolino, R., Curtis-Lake, E., et al. 2023, A&A, 677, A145, doi: [10.1051/0004-6361/202346137](https://doi.org/10.1051/0004-6361/202346137)
- Vijayan, A. P., Lovell, C. C., Wilkins, S. M., et al. 2021, MNRAS, 501, 3289, doi: [10.1093/mnras/staa3715](https://doi.org/10.1093/mnras/staa3715)
- Weigel, A. K., Schawinski, K., & Bruderer, C. 2016, MNRAS, 459, 2150, doi: [10.1093/mnras/stw756](https://doi.org/10.1093/mnras/stw756)
- Williams, C. C., Alberts, S., Ji, Z., et al. 2024, ApJ, 968, 34, doi: [10.3847/1538-4357/ad3f17](https://doi.org/10.3847/1538-4357/ad3f17)
- Windhorst, R. A., Cohen, S. H., Hathi, N. P., et al. 2011, ApJS, 193, 27, doi: [10.1088/0067-0049/193/2/27](https://doi.org/10.1088/0067-0049/193/2/27)
- Windhorst, R. A., Cohen, S. H., Jansen, R. A., et al. 2023, AJ, 165, 13, doi: [10.3847/1538-3881/aca163](https://doi.org/10.3847/1538-3881/aca163)
- Wright, R. J., Somerville, R. S., Lagos, C. d. P., et al. 2024, MNRAS, 532, 3417, doi: [10.1093/mnras/stae1688](https://doi.org/10.1093/mnras/stae1688)
- Yang, G., Caputi, K. I., Papovich, C., et al. 2023, ApJL, 950, L5, doi: [10.3847/2041-8213/acd639](https://doi.org/10.3847/2041-8213/acd639)
- Yue, M., Eilers, A.-C., Ananna, T. T., et al. 2024, ApJL, 974, L26, doi: [10.3847/2041-8213/ad7eba](https://doi.org/10.3847/2041-8213/ad7eba)
- Zavala, J. A., Buat, V., Casey, C. M., et al. 2023, ApJL, 943, L9, doi: [10.3847/2041-8213/acacfe](https://doi.org/10.3847/2041-8213/acacfe)

APPENDIX

A. TABULATED DOUBLE POWER LAW FITS TO THE SMF, SFRF, AGNLF

The parameters of the double power law function (Equation 11) are reported in Table 3.

Quantity	\bar{z}	$\log_{10}(\phi^*)$	α	β	$\log_{10}(x^*)$
M_*	6.488	-2.433 ± 0.067	-0.385 ± 0.073	-2.487 ± 0.128	8.909 ± 0.050
	8.236	-2.822 ± 0.148	-0.475 ± 0.097	-2.039 ± 0.195	8.686 ± 0.124
	10.159	-2.911 ± 0.528	-0.495 ± 0.100	-1.723 ± 0.300	8.383 ± 0.447
	12.563	-2.937 ± 1.208	-0.500 ± 0.100	-2.293 ± 0.523	8.264 ± 0.676
SFR	6.488	-2.776 ± 0.089	-0.543 ± 0.067	-2.432 ± 0.172	0.936 ± 0.066
	8.236	-2.626 ± 0.208	-0.516 ± 0.100	-1.944 ± 0.174	0.440 ± 0.169
	10.159	-3.690 ± 0.171	-0.472 ± 0.098	-2.265 ± 0.473	0.965 ± 0.156
	12.563	-4.148 ± 0.273	-0.498 ± 0.100	-3.210 ± 1.312	0.985 ± 0.198
$L_{\text{AGN}} \text{ uplim}$	6.488	-2.146	-0.471	-1.804	43.318
	8.236	-3.562	-0.598	-1.551	43.663
	10.159	-3.811	-0.522	-1.841	44.194
	12.563	-4.930	-0.504	-2.008	45.021

Table 3. double power law fits (see Equation 11) to the SMF, SFRF and AGNLF. Values are the best fit parameters and the 1σ uncertainties.

B. TABULATED CSMH, CSFH, CAGNH

We fitted `massfunc_snorm_trunc` functions (Eqs. 1-5 in D’Silva et al. 2023c) to the CSFH and CAGNH from $z \approx 0 \rightarrow 13.5$, combining the results of this work and D’Silva et al. (2023c). We fitted with respect to z and use `magemax = 30` and `mtrunc = 2`. The values for the CSMH, CSFH, CAGNH and their fit parameters are reported in Table 4.

Values	\bar{z}	$\log_{10}(\text{CSMH})$	$\log_{10}(\text{CSFH})$	$\log_{10}(\text{CAGNH})$	summed lolim	$\log_{10}(\text{CAGNH}) \text{ uplim}$
-	6.488	6.375 ± 0.029	-1.832 ± 0.037		40.244	41.167
-	8.236	5.839 ± 0.067	-2.163 ± 0.082		39.335	40.217
-	10.159	5.495 ± 0.171	-2.754 ± 0.112		38.844	40.419
-	12.563	5.270 ± 0.553	-3.209 ± 0.193		38.689	40.101
Fit parameters	$\log_{10}(\text{mX})$	<code>mpeak</code>	<code>mperiod</code>		<code>mskew</code>	-
CSFH	-1.077 ± 0.046	1.582 ± 0.182	1.119 ± 0.115		-0.4 ± 0.032	-
CAGNH	41.615 ± 0.052	1.524 ± 0.337	1.141 ± 0.21		-0.365 ± 0.071	-

Table 4. Values and 1σ uncertainties for the CSMH, CSFH and CAGNH (see Equation 12). Values and 1σ uncertainties of the `massfunc_snorm_trunc` parameters.